

Magnesium AZ31 alloy coating for bone implant applications

Francisco Pina Souto de Albuquerque

Thesis to obtain the Master of Science Degree in

Material's Engineering

Supervisors: Prof. João Carlos Salvador Fernandes

Prof. Maria Teresa Moura e Silva

Júri

President: Prof. José Paulo Sequeira Farinha

Prof. João Carlos Salvador Fernandes

Prof. Maria de Fátima G. da Costa Montemor

November 2018

Acknowledgments

I would like to express my gratitude to Professor João Salvador Fernandes, my supervisor, because without his patience and dedication, this work would not be possible.

I would also like to say thanks to my colleagues in the laboratory, Mafalda, Mário, Alberto, Pablo, Raisal, Carmem, Maryna, Lénia, Jeanluca e Mahboobeh because they made this experience a happier one.

I would like to say thank you to Yegor, Kush, Joana and Marta for they were always available to helped me with their scientific knowledge and experience.

My girlfriend Lia, for her support, and my friends always making my life better.

Finally, my deepest gratitude goes to my mother, whom always put me in first place, and without her sacrifice and perseverance, nothing would be possible for me.

Resumo

Biomateriais tem vindo a ser usados no tratamento de vários problemas de carácter médico à algum tempo. Os materiais mais utilizados, hoje em dia, para implantes ortopédicos são as ligas de titânio. No entanto estas ligas apresentam vários problemas relacionados com o efeito *stress shielding*, sintomas de rejeição pelo corpo hospedeiro, como o aparecimento de tecidos necrosados, e os longos períodos que estes materiais ficam dentro dos pacientes podem levar à libertação de substâncias tóxicas, e à necessidade de uma segunda cirurgia.

Vários estudos têm vindo a comprovar a biocompatibilidade das ligas de magnésio e dos seus produtos de corrosão, fazendo das mesmas candidatas promissoras para aplicações ortopédicas. Outra vantagem é o facto de as ligas de magnésio terem propriedades mecânicas similares ao osso cortical, o que reduz vários problemas associados a outros metais.

As altas taxas de corrosão típicas das ligas de magnésio fazem com que as mesmas percam as suas propriedades mecânicas antes do tempo mínimo de 12 semanas, necessárias para a regeneração do osso, ou seja, as mesmas não podem desempenhar as suas funções por tempo suficiente. Outro problema advém das altas taxas de libertação de hidrogénio gasoso, devido às suas reacções de corrosão, adjacente a tecidos moles, que é grande demais porá o nosso corpo lidar, induzindo vários problemas inflamatórios.

O objectivo deste trabalho consiste em revestir a liga de magnésio AZ31 através de uma anodização a plasma, com electrólitos à base de fosfatos, seguido de um tratamento hidrotérmico com EDTA-Ca.

A caracterização dos revestimentos consistiu em microscopia electrónica de varrimento, espectroscopia de difracção electrónica e espectroscopia de raios-X. O comportamento electroquímico foi testado através da técnica de espectroscopia de impedância electroquímica e de curvas de potencial de circuito aberto.

Observou-se um aumento substancial na resistência à corrosão com os revestimentos produzidos, e após a realização do tratamento hidrotérmico e observou-se a existência de uma estrutura em agulha composta por hidroxiapatite.

Palavras Chave: Magnésio, AZ31, implantes biodegradáveis, hidroxiapatite, espectroscopia de impedância electroquímica, potencial de circuito aberto, anodização a plasma, tratamento hidrotérmico, fluidos corporais simulados.

Abstract

Biomaterials have been used for medical treatment of several problems for some time now. And nowadays, most of the bone implant materials are bioinert metals like titanium alloys, however those carry several problems like stress shielding effect, host rejection symptoms like necrosis and, due to the long periods that those materials stay inside the patient's body, the release of toxic substances, may induce the need for a second surgery.

Several studies have proven the biocompatibility of magnesium alloys and their corrosion products, making them promising candidates for biodegradable implant materials. On top of that, magnesium alloys have mechanical properties close to cortical human bone, which would mitigate several bonding and structural problems that arise from other metals.

The high and localized corrosion rates typical of magnesium alloys makes them lose their mechanical properties before the minimum period of twelve weeks needed for the bone regeneration, meaning that those alloys can not perform the bone implant structural function for enough time. Another problem is the high hydrogen release, due to the magnesium corrosion reactions, adjacent to soft tissues, that is too large for our body to deal with, inducing several inflammatory problems.

In this work, an AZ31 magnesium alloy was coated by plasma electrolytic oxidation (PEO) with four different phosphate based electrolytes, and then, hydrothermally treated with two EDTA-Ca solution.

The coatings were characterised by SEM-EDS and XRD, and a good agreement was obtained between those techniques, and hydroxyapatite structures were observed.

The corrosion mechanisms were evaluated through OCP and EIS, showing a substantial decrease in the corrosion rates both in 0.1M NaCl and SBF.

A substantial increase in corrosion resistance and the appearing of needle like hydroxyapatite was observed after the hydrothermal treatment.

Key-words: Magnesium, AZ31, Biodegradable implants, Hydroxyapatite, Electrochemical impedance spectroscopy, Open circuit potential, Plasma electrolytic oxidation, hydrothermal treatment, Simulated body fluids

Contents

Contents.....	XI
1. Introduction.....	1
2. Magnesium as a Biomaterial.....	2
2.1. Historical background	2
2.2. Surface and mechanical properties of magnesium	3
3. Corrosion	4
3.1. Corrosion definition	4
3.2. Forms of corrosion	4
3.3. Corrosion mechanisms	6
3.3.1. Corrosion thermodynamics.....	6
3.3.2. Corrosion rates and measurement	9
3.4. Corrosion behaviour of Magnesium and its alloys	11
4. Corrosion Control.....	13
4.1. Surface modification of Magnesium	13
4.2. Definition of PEO.....	15
4.3. Film formation	16
4.4. Process Parameters.....	17
4.4.1. Solution composition and concentration	19
4.5. Hydrothermal treatment.....	20
5. Characterization techniques	21
5.1. Electrochemical Impedance Spectroscopy	21
5.2. Scanning Electron Microscopy	24
5.3. X-ray Diffraction Spectroscopy	26
6. Materials and methods	28
6.1. Plasma Electrolytic oxidation.....	28
6.2. Hydrothermal treatment.....	31
6.3. Thickness measurement.....	32
6.4. Electrochemical Impedance spectroscopy	32
6.5. Scanning Electron Microscopy	33
6.6. X – ray diffraction	33
7. Results	34
7.1. Thickness measurement.....	34
7.2. Morphology and microstructure	35
7.3. Electrochemical Behaviour	42
7.3.1. Immersion in 0.1M NaCl and EIS.....	42
7.3.2. Immersion in SBF and EIS of PEO coated samples.....	50

7.3.3.	Immersion in SBF and SBF of Hydrothermally treated samples	55
8.	Conclusions and future work.....	59
9.	References	61

Tables list

Table 1 - Human bone mechanical properties. Adapted from [7, 8].....	3
Table 2 - Electromotive force series. Adapted from [16]	7
Table 3 - Chemical potential for Mg and some Mg compounds. Adapted from [22]......	11
Table 4 - Impedance of common equivalent circuits. Adapted from [44].	24
Table 5 - Nominal composition of AZ31 wrought alloy. Adapted from [51]......	28
Table 6 - Solutions used in the MAO treatment.....	30
Table 7 - Plasma electrolytic oxidation programs.....	30
Table 8 – Overall view of the Plasma Electrolytic Anodization for all samples.	30
Table 9 - Experimental conditions of the HT treatments	32
Table 10 - Working electrodes exposed areas on the 2 ^o round of impedances.	33
Table 11 - Comparison of ionic charges of SBF and human blood plasma. Adapted from [52].....	33
Table 12 - Average thickness obtained for anodized samples.....	34
Table 13 - Average thicknesses obtained for samples 2B and 4B after three days of SBF immersion, and of hydrothermally treated samples. Before and after SBF immersion.....	34
Table 14 - Atomic percentages of all PEO coatings.....	37
Table 15 - EDS results of hydrothermally treated samples	39
Table 16 - EDS results for samples after immersion in SBF.	41
Table 17 - Fitting results for the bare alloy and coated samples.	49
Table 18 - Equivalent circuit fitting results.....	54
Table 19 - Fitting results for samples 2BHt ₁ and 4BHt ₂	58

Figures List

Figure 1 - Pourbaix diagram for magnesium. [17]	8
Figure 2 - Polarization curve of a metal. Adapted from [15].	10
Figure 3- Magnesium corrosion mechanisms.[17].....	12
Figure 4 – Schematic drawing of conversion coating types.[24]	14
Figure 5 - Schematic representation of a PEO experimental set up. 1 – power supply; 2 – refrigerator; 3 – Container and counter electrode; 4 – working electrode; 5 – solution stirrer; 6 – Fume extraction vent. Adapted from [26].	19
Figure 6 - Growth mechanism of HAp coatings with hydrothermal treatments on bare Mg [43].	21
Figure 7 - Example of a Nyquist plot.[13].....	22
Figure 8 – Example of Bode (left) and phase angle plots (right). Adapted from. [18].....	22
Figure 9 - Schematic representation of a potentiostat working principles [44].....	23
Figure 10 - Schematic representation of the SEM principles [48].	25
Figure 11 - Schematic representation pf Bragg's law. [51]	27
Figure 12 - Samples used before treatment.....	29
Figure 13 -Experimental set up for the PEO treatment.....	29
Figure 14 - Experimental hydrothermal treatment set up.	31
Figure 15 - SEM micrograph of sample 1A 200x.	35
Figure 16 - SEM micrograph of sample 1B 200x.	35
Figure 17 - SEM micrograph of sample 2A 200x.	36
Figure 18 - SEM micrograph of sample 2B 200x.	36
Figure 19 - SEM micrograph of sample 3A 200x.	36
Figure 20 - SEM micrograph of sample 3B 200x.	36
Figure 21 - SEM micrograph of sample 4A 200x.	36
Figure 22 - SEM micrograph of sample 4B 200x.	36
Figure 23 – SEM micrograph of sample 2BHt ₁ 100x.	38
Figure 24 - SEM micrograph of sample 2BHt ₁ 5000x.....	38
Figure 25 - SEM micrograph of sample 2BHt ₂ 50x.....	38
Figure 26 - SEM micrograph of sample 2BHt ₂ 5000x.....	38
Figure 27 - SEM micrograph of sample 4BHt ₁ 100x.	38
Figure 28 - SEM micrograph of sample 4BHt ₁ 5000x.....	38
Figure 29 - SEM micrograph of sample 4BHt ₂ 50x.....	39
Figure 30 - SEM micrograph of sample 4BHt ₂ 5000x.....	39
Figure 31 - XRD patterns of bare alloy and Ht samples before the immersion test. \diamond - HAp; \bullet – α -Mg; \circ – MgO.	40
Figure 32 – 2BHt ₂ after 72 h of SBF immersion.....	41
Figure 33 - 4BHt ₁ after 72h of SBF immersion.....	41
Figure 34 - XRD diffractograms of Ht samples after the immersion test; \diamond - HAp; \bullet – α -Mg; \circ – MgO; \square – Mg(OH) ₂	42
Figure 35 – Picture of sample 1A before the 24h immersion in 0.1M NaCl	43
Figure 36 - Picture of sample 1A after the 24h immersion in 0.1M NaCl	43
Figure 37 - Picture of sample 1B before the 24h immersion in 0.1M NaCl	43
Figure 38 - Picture of sample 1B after the 24h immersion in 0.1M NaCl	43
Figure 39 - Picture of sample 2A before the 24h immersion in 0.1M NaCl	43
Figure 40 - Picture of sample 2A after the 24h immersion in 0.1M NaCl	43
Figure 41 - Picture of sample 2B before the 24h immersion in 0.1M NaCl	44
Figure 42 - Picture of sample 2B after the 24h immersion in 0.1M NaCl	44
Figure 43 - Picture of sample 3A before the 24h immersion in 0.1M NaCl	44
Figure 44 - Picture of sample 3A after the 24h immersion in 0.1M NaCl	44
Figure 45 - Picture of sample 3B before the 24h immersion in 0.1M NaCl	44
Figure 46 - Picture of sample 3B after the 24h immersion in 0.1M NaCl	44
Figure 47 - Picture of sample 4A before the 24h immersion in 0.1M NaCl	45
Figure 48 - Picture of sample 4A after the 24h immersion in 0.1M NaCl	45

Figure 49 - Picture of sample 4B before the 24h immersion in 0.1M NaCl	45
Figure 50 - Picture of sample 4B after the 24h immersion in 0.1M NaCl	45
Figure 51 - Nyquist plots of bare metal and coated samples.	46
Figure 52 - Bode plots of bare metal and MAO coated samples.	46
Figure 53 - Equivalent circuit proposed for the bare alloy.....	47
Figure 54 - Equivalent circuit proposed for all the coated samples.	48
Figure 55 - Fitting results for sample 4B (red) and 2B (Blue).	48
Figure 56 - 2B after the 72h immersion in SBF	50
Figure 57 - 4B after the 72h immersion in SBF	50
Figure 58 – 2BHt ₁ before the 72h immersion in SBF	50
Figure 59 – 2BHt ₁ after the 72h immersion in SBF.....	50
Figure 60 – 2BHt ₂ before the 72h immersion in SBF	51
Figure 61 – 2BHt ₂ after the 72h immersion in SBF.....	51
Figure 62 – 4BHt ₁ before the 72h immersion in SBF	51
Figure 63 – 4BHt ₁ after the 72h immersion in SBF.....	51
Figure 64 – 4BHt ₂ before the 72h immersion in SBF	51
Figure 65 – 4BHt ₂ after the 72h immersion in SBF.....	51
Figure 66 – 12h OCP for samples 2B and 4B immersed in SBF	52
Figure 67 – OCP curve one hour before each EIS in sample 2B and 4B	52
Figure 68 - 2B Nyquist plots for impedance in SBF.....	53
Figure 69 - 2B Bode plots for impedance in SBF	53
Figure 70 - 4B Nyquist plots for impedance in SBF.....	53
Figure 71 - 4B Bode plots for impedance in SBF	53
Figure 72 - Equivalent circuit proposed to fit the data of samples 2B and 4B immersed in SBF.....	54
Figure 73 - 12h OCP for samples 2bht ₁ 4bht ₂ immersed in SBF	55
Figure 74 - OCP curve one hour before each EIS in sample 2BHt ₁ and 4BHt ₁	56
Figure 75 - 2BHt ₁ Nyquist plots for impedance in SBF.....	56
Figure 76 - 2BHt ₁ Bode plots for impedance in SBF	56
Figure 77 - 4BHt ₂ Nyquist plots for impedance in SBF.....	57
Figure 78 - 4BHt ₂ Bode plots for impedance in SBF	57
Figure 79 - Equivalent circuit proposed for fitting impedance data of samples 2BHt ₁ and 4BHt ₂	57

List of abbreviations and symbols

Alternating current	AC
Auger electrons	AE
Anodic hydrogen evolution	AHE
Backscattered electrons	BSE
capacitance	C
Cathodic hydrogen evolution	CHE
Constant phase element	CPE
Cathode ray tube	CRT
Direct current	DC
Duty cycle	dc
Energy dispersive X-ray spectroscopy	EDS
Electrochemical impedance spectroscopy	EIS
Electromotive force	emf
Pulse energy	E_p
Faraday constant	F
Hydroxyapatite	HAp
Hydrothermal treatment	Ht
Current density	i
Electrical current	I
Corrosion current	i_{corr}
energy	J
Inductance	L
Micro-arc oxidation	MAO
Magnesium	Mg
Primary electrons	PE
Plasma electrolytic oxidation	PEO
resistance	R
Intermediary species resistance	Rad
Charge transfer resistance	Rct
HAp coating pore resistance	RHAp
PEO coating pore resistance	Rpo
Solution resistance	Rs
Simulated body fluids	SBF
Secondary electrons	SE
Scanning electron microscopy	SEM
time	t
Pulse on time	T_p
Potential	V
x-ray diffraction spectroscopy	XRD
Impedance	Z
Gibbs free energy difference	ΔG
Phase displacement	θ
Wave length	λ
Frequency	ω

1. Introduction

Biomaterials are man made or natural origin materials that scope the substitution, repairing or augmenting human body parts. However, we shouldn't think that the replacement of an organ or bone by an artificial one would be more effective since our body is the result of millions of years of evolution, therefore, the human body will always be healthier and more efficient than with replaced parts [1].

When thinking about bone repairing, first, one should always look at the important properties and constraints that the material must fulfil. The physical mechanical properties, that include density, tensile and compressive strength, toughness, fracture and fatigue resistance and hardness, are of critical importance because they will decide if the material is strong enough to withstand all the mechanical stresses imposed by their use, however it cannot be too strong, in order not to induce stress shielding, i.e. the bone reabsorption due to excess of protection. The chemical surface properties, like corrosion resistance, are also of main importance, since electrochemical reactions may release several toxic and hazardous species, and obviously, decrease the mechanical attributes of the material. Bioactivity, i.e. the reaction that the body may have upon the implant, is also of critical importance since the body reaction with the material, or the corrosion products and debris released by the material, may lead to rejection or to the need of implant removal surgery [2].

Understanding of the bone is also, obviously, of main importance, which will be explained with more detail in section 2.2. Since the implant surface is the place where the reactions between the body and the implant will take place, for bone repairing, the main properties of an implant are osteointegration, that will be decided by the material's cellular adhesion, osteoconduction, which will provide a scaffold for the bone growing through direct bonding, and osteoinduction, meaning to induce the formation in non osseous sites [2, 3].

There are two main groups of bone implants, bio-inert and bio-degradable ones. The first ones are used nowadays with great success rates. However, because most of the times they stay inside the human body for long periods, they carry the problem of often needing a second surgery, for removal, due to immunologic responses of the human body, which increases the suffering level and time for the patients and the costs for health care systems. Bio-degradable ones are replaced, with time, by the healthy regenerated bone or tissue in cause, thus the goal of this implants is to provide mechanical support for the growing new bone, and disappear releasing nontoxic products after the injury recovery [3].

The most effective materials for bone implants, nowadays, is autologous bone or autograft, which is the use of transplanted trabecular, cortical or a composite of both, from one body part to another, although creating major problems like donor site morbidity and limited bone supply. One option for solving this drawback is the use of allograft, cortical bone from an external donor. However, it is usually harvested from cadavers, and if it is used frozen or demineralized, it has limited osteoconductivity. And when it is used as fresh, it still has some important drawbacks, like bacterial infection or disease transmissions, immune response, non-union, due to different bone qualities, and so on [3, 4].

Because, even with all those drawbacks mentioned before, autologous bone is, still, the election material for bone healing, there is a major effort to improve synthetic scaffolds for human bone growing. Those

are divided in natural or synthetic polymers, ceramics, like bio glasses, calcium-phosphates and others, metals, and composites [4].

Polymers used as biomaterials such as collagen (natural) or poly-lactic acid (PLA) tend to have good biocompatibility and cell adsorption, however they tend to degrade too fast in physiological environment and have inferior mechanical properties. Ceramics, like hydroxyapatite (HAp) or silicate bioactive glasses, have a good biocompatibility, mechanical properties and high corrosion resistances, but tend to be brittle and have a low fracture toughness. Metals have good mechanical properties and biocompatibility, unfortunately they tend to release toxic ions into the body and induce bone shielding effect. Composite materials, like HA-coated metal, can combine several advantages of the metals and ceramics classes [4, 5].

Magnesium (Mg), and its alloys have a high potential to be useful in biomedical applications due to its corrosion products (Mg^{2+}) being easily removed by the urinary system. However, despite of having superior mechanical properties compared to other biodegradable materials, magnesium alloys have high corrosion rates, which leads to a fast loss of their structural properties [3].

The scope of this work is to tailor Mg alloy AZ31 surface through Plasma-electrolytic Oxidation (PEO) followed by a hydrothermal treatment, aiming to control its dissolution rate, making it possible to be used in bio-degradable orthopaedic material.

2. Magnesium as a Biomaterial

2.1. Historical background

Magnesium was first isolated by Sir Humphrey Davy in 1808. In 1822, Sir Davy's assistant, Michael Faraday, produced metallic Mg by electrolysis of fused anhydrous magnesium chloride. In 1852, Robert Bunsen started producing metallic Mg, by electrolysis, for commercial purposes, by the first time. Edward C. Huse used an Mg alloy ligature to stop bleedings in 1878. In 1900, Erwin Payr used pure Mg tubes to connect intestine parts and blood vessels, his reports inspired several scientists and in 1906 Albin Lambotte started to investigate Mg as an implant material both in humans and animals, discovering that in rabbits and dogs the total absorption of Mg happens between seven and ten weeks. After, Lambotte recommended the use of Magnesium in several types of bone fractures. Several authors also condemned Mg due to its fast corrosion rate, making it not suitable for structural applications in physiological environments, and its gas evolution. After that, authors have proven that Mg corrodes at different rates in different parts of the body, making it possible the successful use of pure Mg as a connector for intestinal anastomosis. After that, some authors shown that Mg corrosion products didn't have any hazardous or toxic effect. But for structural bone implant applications, the corrosion rate still

to high. Since then, there has been a major effort for controlling Mg alloys corrosion rate and promote its biological performance, thus enabling its use as an orthopaedical material [6].

2.2. Surface and mechanical properties of magnesium

Human bone is a composite consisting in an inorganic phase, HAp, and an organic one, composed by type I, III, and IV collagen and fibrillin. Bone has a hierarchical structure, composed by cancellous (trabecular) bone in the inside, which is a porous network of trabeculae, and compact (cortical) bone, with a porosity of less than 5%. However, at a micro/nanoscale, either one of those parts of human bone is composed by type I collagen reinforced with nanocrystals oriented according with the axial direction of hydroxyapatite. Table 1 summarizes the main mechanical properties of human bone and AZ31 magnesium alloy [3].

Table 1 - Human bone mechanical properties. Adapted from [7, 8].

	Density (g/cm ³)	Yield strength (MPa)	Tensile strength (MPa)	Young Modulus (GPa)
Cortical Bone	1.8 - 2.1	110 – 130	35 - 283	17 - 20
Trabecular Bone	-	-	1.5 - 38	0.5 - 3
AZ31	1.78	263	263	45

The main failure reason for bone implants can be mechanical, due to the Young Modulus mismatch, that can lead to a stress-shielding effect, low fracture toughness and low fatigue strength. Chemically, having a high corrosion rate, can lead to an implant failure due to the release of toxic corrosion products, and the appearance of fibrous tissue as an immunologic response can avoid a proper bond between bone and implant [7, 9].

Comparing magnesium alloys with other classes of materials, magnesium presents several advantages, like an elasticity modulus close to cortical bone, fracture toughness superior to any bio ceramic, superior yield strength than most polymers. But the fast corrosion rate of magnesium in chloride containing electrolytes, like the body fluids, or blood plasma, releases amounts of gaseous hydrogen that will delay the healing process, and induce necrosis in the surrounding tissues, induce large variations on local pH, associated with cell death and finally, the fast corrosion rate can induce the rapid loss of mg alloys mechanical properties, leading to the implant premature failure [10].

The human healthy intake of magnesium is of about 300 – 400mg per day, and its corrosion products, like bivalent Mg ions, are considered to be physiological beneficial for several metabolic processes and apatite forming, and any excess can be efficiently excreted in the urine [11].

3. Corrosion

3.1. Corrosion definition

The term corrosion is used to describe the degradation of a material's surface due to the contact with a corrosive media. There are several definitions for this kind of phenomena including the IUPAC definition, "Corrosion is an irreversible interfacial reaction of a material (metal, ceramic, and polymer) with its environment which results in consumption of the material or in dissolution into the material of a component of the environment", and the ISO 8044-1986, "Physicochemical interaction between a metal and its environment which results in changes in the properties of the metal and which may often lead to impairment of the function of the metal, the environment, or the technical system of which these form a part" [12].

Corrosion can happen through physical, chemical and electrochemical processes. Physical processes include the degradation of solid metals in contact with liquid ones due to the penetration of liquid metal on the grain boundaries or just the dissolution of a solid metal in a liquid, forming an alloy. Chemical corrosion is the degradation phenomena without the electric current generation, for example, a metallic surface attack through etching, or the contact with dry gases, or non-electrolytes. Electrochemical mechanisms of corrosion involve anodic and cathodic reactions happening at the same time. The anodic dissolution of a metal involves the release of metal cations onto the electrolyte while electrons flow through the metal to feed the cathodic reaction of electrolyte reduction [12].

This happens due to the second principle of thermodynamics, which states that "matter always tends to a maximum state of entropy". And knowing that metals have an organized crystallographic structure, it is easy to understand why corrosion exists in metals[13] .

As in any other chemical reaction, the reaction between a metal and its environment will only take place if it lowers the Gibbs free energy of the entire system. The tendency of a metal to corrode will depend of its difference of Gibbs free energy (ΔG), i.e., according to the third principle of thermodynamics "a given system always tends to minimize its free energy".

3.2. Forms of corrosion

Corrosion damage in metals can happen in several forms, and those are classified according to the appearance of the material, and changes on its properties, and, aiming to predict the corrosion behaviour of an engineering metal, one must take into account six main factors. Those are the material itself, its chemistry, crystal structure and surface condition; The environment, composition, diffusion,

hydrodynamic conditions; Stresses subjected, cyclic, intentional, residual, thermal, among others; Geometry of the part itself, discontinuities, galvanic potentials, restrictions in species diffusion; Temperature and time [13].

The most important forms of corrosion are uniform attack or general corrosion, galvanic corrosion, pitting corrosion, dealloying, intergranular corrosion and stress corrosion cracking.

- General or uniform corrosion is a type of corrosive attack in which a large fraction of the area is homogeneously affected. This type of corrosion is measured with the amount of material lost. It is easily measured and identifiable, and because there is a large area being affected, its depth is, usually, too small to induce structural damages. However, if it is not controlled, due to the increasing roughness of a surface, it can lead to other, more dangerous, types of corrosion. [13, 14, 15].
- Galvanic corrosion occurs between two dissimilar metals, dissimilar grains in a metal (micro galvanic corrosion) and due to the presence of intermetallic compounds or impurities. Due to different galvanic potentials, the nobler one becomes the cathode, and the more active one acts as an anode. Obviously, the difference in areas is of vital importance since the total current flow of an electrolytic cell must be equal in both sites, and it can lead to other types of corrosion damage, like crevice or stress corrosion cracking, that will be explained later in this section [13, 14, 15].
- Pitting corrosion is a localized attack, it usually takes the form of a small and deep hole on the surface, turning difficult the diffusion of species to or from that place, meaning that it will happen in relatively small and confined areas, and, since the absolute current must be equal in both anodic and cathodic sites, the rate of penetration will be faster than most types of corrosion. This type of corrosion damage is among the most dangerous ones, because it is easily hidden by its products, or by mechanical junctions. Pits, on a material surface can also act as “seeds” for other types of corrosion attack since they are points of stress concentration. Pits can appear due to several factors, some of them are a localized fracture on the protective film of a metal, the relative motion between two surfaces can lead to a series of pits – fretting corrosion. The exposure to gas bubbles can also lead to a series of pits on a metal – cavitation. Or between mechanical joints, as it makes difficult the change of media on that localized spot – crevice corrosion [13, 14, 15].
- Dealloying corrosion happens when one element is corroded with preference to others, meaning that the alloy will remain apparently intact, however with a porous structure, and therefore with its mechanical properties damaged. Types of this corrosion form are dezincification, as in brasses in which their zinc is corroded, and parting, in which the most reactive elements are completely corroded, and the remain is purified [13, 14, 15].
- Intergranular corrosion happens in grain boundaries, where the metal is more reactive due to segregation phenomena or mismatches between adjacent grains. This type of attack because the grain boundary is more active, acting as an anode, that the grain bulk, that acts as a cathode. Because there is a large difference of areas, the rates of corrosion happen fast, leading to catastrophic failure, if not controlled. However, in magnesium and its alloys, the interior of its

grains tend to be less noble than its grain boundaries, resulting in the undercutting of an entire grain, instead of the loss of mass inside the grain [13, 14, 15].

- Stress corrosion cracking (SCC) is the result of both the corrosion and external stresses. It happens when a metal is subjected to tensile stresses, repeated or alternated, in a corrosive environment, resulting in failure way below the fatigue resistance in a corrosive media. The failure occurs in stress concentration sites, created by corrosive attack due to any other reason [13, 14, 15].

3.3. Corrosion mechanisms

Due to the phenomena above described, the surface atoms of a given metal will leave their place on the metal structure and pass on to the electrolyte in the form of cations. The equation below describes the anodic reaction that happens on the surface.



When this happens, the metal surface gets positively charged while the electrolyte gets more negative, meaning that while the metal is oxidized, cathodic reactions will occur on the electrolyte. The electrodes that more common in corrosion of metals are the oxygen and hydrogen electrodes.

Cathodic reactions are more difficult to understand since they depend of environment parameters, like pH, temperature, composition, and others.[15]

Equation 2 shows the equilibrium for the Hydrogen electrode, in which gaseous hydrogen forms.



And for the Oxygen electrode in acid solutions (3) and alkaline or neutral solutions (4).



3.3.1. Corrosion thermodynamics

The ΔG of an electrochemical reaction can be given by equation 5, in which n is the number of electrons, E is the cell potential or electromotive force (emf), and F is the Faraday's constant [15].

$$\Delta G = -nEF$$

5

The free energy change is given by the difference between the cathode and the anode reduction and oxidation potentials.

The redox potential of a metal is the difference between the metal and its neutral state, and usually measured against a standard hydrogen electrode, therefore the free energy change can be given by the equation 6 [15].

$$E = E(\text{cathode}) - E(\text{anode}) \quad 6$$

The more negative the standard potential of a given metal is, more reactive it will be, meaning that it has more tendency to corrode (behave as an anode). Table 2 lists all metals ordered by their standard potentials.

Table 2 - Electromotive force series. Adapted from [16]

Electrode reaction	Standard Potential at 25°C (Volt)
$Au^{3+} + 3e^{-} = Au$	1.52
$O_2 + 4H^{+} = 2H_2O$	1.299
$Ag^{+} + e^{-} = Ag$	0.799
$Cu^{2+} + 2e^{-} = Cu$	0.340
$2H^{+} + 2e^{-} = H_2$	0
$Ni^{2+} + 2e^{-} = Ni$	-0.257
$Fe^{2+} + 2e^{-} = Fe$	-0.44
$Zn^{2+} + 2e^{-} = Zn$	-0.76
$Cr^{2+} + 2e^{-} = Cr$	-0.90
$Ti^{2+} + 2e^{-} = Ti$	-1.63
$Al^{3+} + 3e^{-} = Al$	-1.67
$Mg^{2+} + 2e^{-} = Mg$	-2.34
$Li^{+} + e^{-} = Li$	-3.045

A galvanic cell consists in two electrodes immersed in an electrolyte and connecting those electrodes with a conductor wire, an electric current will pass from the negative to the positive pole, meanwhile, in the electrolyte, both negative and positive carriers flow. The amount of charge carried through the wire must be equal to the total charge transferred through the electrolyte, on the opposite way. Being the total current flow given by the Ohm's law given in equation 7 [14].

$$I = \frac{E}{R} \tag{7}$$

Despite of providing information about the driving force of corrosion, emf series are limited since some metals tend to form a protective layer of oxides, which will shift their position in to a more noble one, for example, Aluminium and Chromium are active metals, but due to the spontaneous formation of a protective oxide layer (passivation), in specific solutions, their rate of corrosion will be inferior, making them more resistant.

Another useful tool for predicting the potential of a corrosion reaction to occur is the Pourbaix diagram, as shown in figure 1. Unlike emf series, that assume the potentials for metals in equilibrium with ions of the same species, Pourbaix diagrams (or E-pH) provides information of reaction potentials and possible products, in aqueous solutions plotting the reaction potential against the pH of the solution.

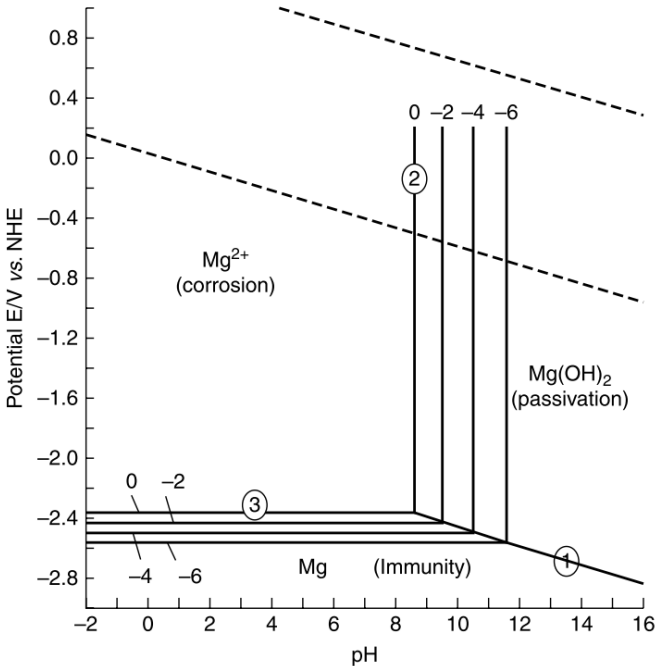


Figure 1 - Pourbaix diagram for magnesium. [17]

The lines in the E-pH diagram represent equilibrium condition for a reaction, if a line is vertical, then the reaction is not influenced by the potential applied, and if it is horizontal, then the pH of the solution

adjacent to the electrode does not influence the reaction, meaning that there is no H⁺ or OH⁻ involved in the reaction.

Each domain represents the conditions in which a species is more stable, for example, at high pH, with no potential applied, Mg(OH)₂ is the stable compound, if the potential decreases, some hydrogen evolution can be seen, and if the pH decreases, Mg(OH)₂ will dissolve, and Mg²⁺ will stay in solution, meaning that the metal is corroded [14].

These diagrams are useful to predict in which domain a metal is stable in its metallic phase, and which oxides will form considering the potential applied and pH of the solution. Cathodic protection techniques use E-pH diagrams to maintain the metal in its immunity domain, other make use of oxides domains in order to create a protective oxides layer [14].

Like emf series, these diagrams are made of thermodynamic data, therefore they do not provide information about rates of corrosion.

3.3.2. Corrosion rates and measurement

Corrosion rate is defined as the amount of corrosion that happens to a material per unit of time, for example the difference in mass of a material per unit of time [18]. Faraday's laws states that in anodic reactions, the weight of material lost is proportional to the current density through the electrode as in equation 8 where m is the mass of the anode, M is its molar mass, t is time, n is number of electrons involved and F is Faraday's constant [19].

$$\Delta m = i \frac{M \Delta t}{nF} \quad 8$$

When current flows to or from an electrode, the potential measured will change in the opposite way of the current flow, meaning that the anode will become more cathodic and the cathode more anodic, decreasing the difference in potential between both half cells. This potential change is called polarization [14].

There are three types of polarization. The first one is called potential drop, and is a consequence of several factors, like the metal itself, electrolyte resistivity, protective layers on the surface, among others and it happens when current passes through any interface. The second is Concentration polarization, and it is caused by the change on concentration of ions close to the electrodes surface. Its limited by the diffusion coefficient, and the current at which the loss of ions consumed is higher than the defunded from the bulk to the surface, is called the limiting current, in which the electrode potential tends to infinite.

The third one is activation polarization. The reactions that occur in both electrodes have different rates, meaning that to have the same rate of reaction, a higher potential is needed, this difference is called overvoltage.

Plotting the potential against the current, like in figure 2, one can see that the potential increases with the increasing current. Applying a cathodic potential will result on the curve CD, and an anodic one in the curve AB. If sufficient anodic current is applied, then, the cathodic reaction becomes insignificant relative to the anodic current, meaning that the current density is equal to the anodic current density. Extrapolating the linear part of both curves, and intersecting them, we obtain the Tafel slope, and the intersection will give us the corrosion current (i_{corr}), that is, the current density at which the system is on short-circuit, meaning a freely corroding situation [20].

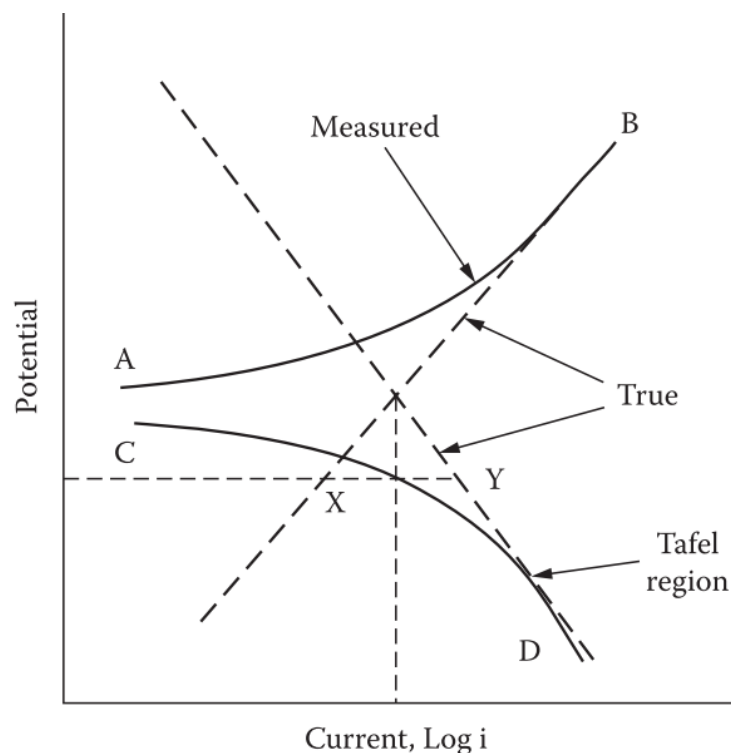


Figure 2 - Polarization curve of a metal. Adapted from [15].

Polarization techniques often use direct current (DC), however there is a number of complications that arise from those methods. One source of errors is the ohmic resistance of the solution, that increases the potential needed for reactions to occur, being this potential algebraically added to the potential applied. Other source of error arises from diffusion controlled processes, meaning that concentration of certain species can decrease or increase the corrosion potential, making the overall reaction dependent of diffusion and hydrodynamic conditions [9,12]. DC methods are also highly dependent on the scan rate at which those are performed, since the changes in potential induced has to be slow enough to

keep the adsorbed or formed species on the surface, that have the behaviour analogous to a capacitor, fully charged, otherwise the polarization measured will not represent the corrosion mechanism [13].

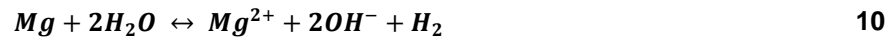
3.4. Corrosion behaviour of Magnesium and its alloys

As it is shown before in table 2, magnesium (and its alloys) is a very active metal when comparing to others, meaning that it has a great tendency to be oxidized. This is supported by the thermodynamic data in table 3, which shows the chemical potential for some of its oxides and hydroxides [22].

Table 3 - Chemical potential for Mg and some Mg compounds. Adapted from [22].

Specie	Oxidation state	μ_0 (kcal/mol)
Mg	0	0
Mg⁺	+1	- 61
Mg²⁺	+2	-109
Mg(OH)₂	+2	-199
MgH	-1	+34
MgH₂	-2	-8
MgO	+2	-136

As it is shown by the above table, Mg compounds are much more stable than its metallic form, meaning that when exposed to a neutral environment or water, its surface tends to be covered in oxides and hydroxides. As it can be seen in the Pourbaix diagram in section 3.3.1., only at very low potentials Mg's metallic form is stable, which is very rare to happen in nature. Equations 9 and 10 are the main overall oxidation reactions of magnesium in acidic and neutral or alkaline environments, respectively [17, 22].



The above equations show that for each Magnesium atom dissolved a molecule of hydrogen is generated, and for neutral or alkaline environments, two OH⁻.

Hydrogen evolution can increase the local concentration of protons adjacent to the corroding area, decreasing the concentration effect on polarization, which can increase the corrosion rate. It also makes it hard for corrosion products to precipitate on a corroding area, meaning that the oxides film of the surface will be loose and won't provide protection, unlike aluminium passive films. However, as it is seen in the E-pH diagram in the previous section, in both acid and basic solutions, there will be an increase in local pH, alkalinisation, until 10.5, when the consumption of protons by HE and formation OH⁻ will be equal to the consumption of OH⁻ by the formation and deposition of magnesium hydroxides on the surface. And this local alkalinisation adjacent to the magnesium surface can lead to cellular death in the tissues adjacent to the implant [23].

The hydrogen evolution is present in both the cathodic (CHE) and anodic (AHE) reactions, and the amount of hydrogen created is proportional to the weight loss in Mg and Mg alloys. In figure 3 its magnesium corrosion, hydroxides generation and both anodic and cathodic HE as explained above in the Pourbaix diagram on figure 1 [17].

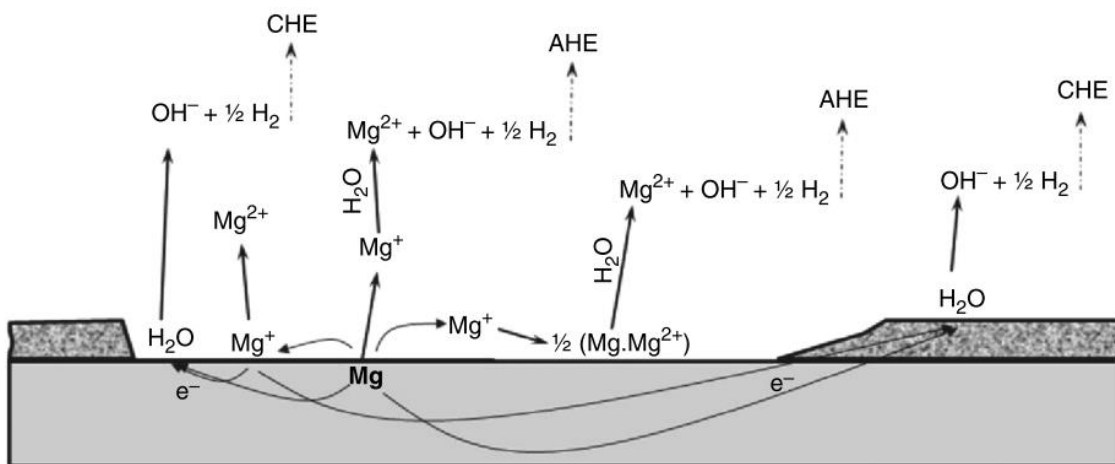


Figure 3– Magnesium corrosion mechanisms.[17]

4. Corrosion Control

When an implant is used to heal a bone fracture, firstly, the body will react to the foreign body. In this inflammatory phase, the response of the initial surrounding tissues will decide if the implant will or not be rejected, therefore, during that time of about three to seven days, the material is required to perform a suitable substrate for the growing of new tissues. The second phase of the healing process is the reparative phase, in which new bone grows with the slow degradation of the implant and occupies its place. This phase takes about three to four months during which the material must keep providing a structural function while the bone is healing and still can't perform its own structural requirement. An effective implant must withstand these requirements at least for twelve weeks, so the human body enters in the final healing stage, the remodelling, that takes from a few months to years to complete. [10]

Since degradation will occur, it is of vital importance to minimize hazard effects of elements going into the human bone and blood stream, such as aluminium, that is linked to Alzheimer's disease and accumulates in the bone decreasing the osteoblasts viability. Excess of calcium can lead its accumulation in the kidneys (stones), copper, manganese, lithium, among other species are linked to several neurologic diseases and harmful effects.

Due to its non-toxicity to the human body, magnesium and its alloys are suitable candidates for biodegradable implants, however, due to its high corrosion rates, if untreated, magnesium alloys will release toxic species to the host body at a rate that our metabolism can't process and expel them. [10] Hence the need for corrosion resistance enhancement.

4.1. Surface modification of Magnesium

Aiming to control the corrosion of magnesium alloys, several techniques were proposed for the deposition of polymeric coatings.[24, 25].

Magnesium alloys can be divided in four groups. Pure Magnesium, aluminium containing alloys, like AZ31 and AZ91, rare earth containing alloys, like AE21 or WE43, and aluminium free alloys like MgCa 0.8 or MgZn6. Alloying can improve several properties like the formability to ease production processes or mechanical strength through grain refinement or the formation of intermetallic phases [8]. However, alloying can improve several properties like corrosion resistance, or strength through grain refining. But, as it was explained before, most of the elements can be toxic for the human body, therefore, several surface treatments were proposed.

Surface enhancement can be achieved through mechanical and chemical methods. Mechanical methods consist in rolling, shot peening, milling at low speeds the material's surface, changing the topography, improving cell adhesion and osteointegration. Chemical treatments can be divided in deposited coatings and chemical conversion coatings.

The first group consists in cover the surface of the sample with metallic, inorganic or organic coatings. However metallic coatings present disadvantages in bio applications since galvanic corrosion becomes a serious problem when the coating is damaged, which is not acceptable in a human environment. The deposition of inorganic coatings by physical techniques like plasma spraying or laser application and from gas phases present problems with complex geometries, high energy consumption and complex facilities. The deposition of organic coatings usually happens trough techniques like deep coating, thiscoatings offer several advantages not only in corrosion protection, but also in easiness in fictionalizing with large biomolecules.

Other techniques for deposition of this types of coatings, or composites coating made from inorganic and organic layers are cathodic electrodeposition, mainly used for inorganic coatings, sol-gel techniques, however those have to be repeated several times to produce a coating with enough thickness for an efficient corrosion protection.

Chemical conversion coatings are those that appear due to chemical reactions between the substrate, usually a metallic one, creating, in most of the cases, an oxides layer through a chemical or an electrochemical process. Unlike deposition techniques, the majority of coatings produced this way is inorganic, exhibiting a ceramic like behaviour. In figure 4, a schematic drawing of the types of conversion coatings used nowadays.

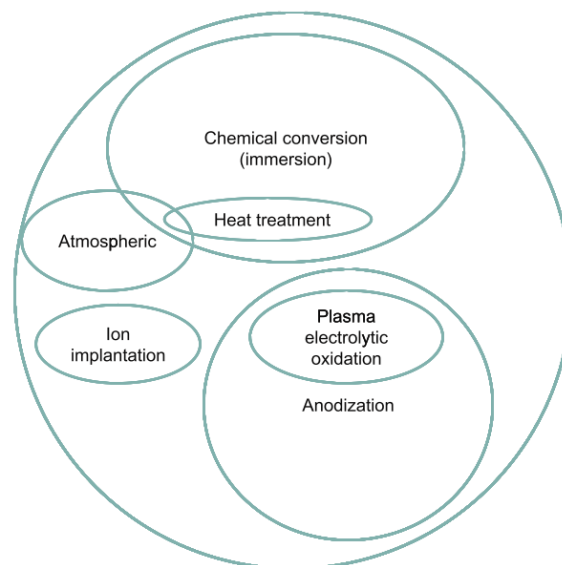


Figure 4 – Schematic drawing of conversion coating types.[26]

Anodization consists in creating an anodic oxides layer on the substrate, thus forming an isolating barrier between the metal and he atmosphere. A special type of anodization is the Plasma electrolytic anodization, in which the breakdown potential is achieved, creating a porous layer. In the next sections, both techniques will be explained with further detail.

Ion implantation techniques have shown thicknesses of about one μm , and in a few experiments, the treatment decreased the corrosion resistance [26].

Chemical immersion methods, that were explained before, can also change the surface of the metal, and a specific type of this technique is the hydrothermal treatment, that is used to seal the pores of other methods. This technique will be explained in further detail in section 4.5.

4.2. Definition of PEO

Plasma Electrolytic Oxidation (PEO), also known as Micro-Arc Oxidation (MAO), is a type of anodization that uses higher voltages and so it produces thicker and more porous coatings. As anodization, PEO is also a conversion coating, i.e., a coating that results from chemical or electrochemical reactions between the substrate and the environment [26]. Therefore, before engaging with PEO itself, one must first understand the basics of anodization processes.

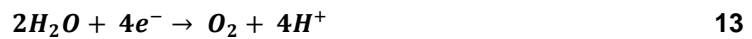
Anodization is a surface tailoring technique that consists in immersing the substrate in an electrolyte, and the application of a voltage, resulting in a compact layer of oxides on top of the metal surface.[26] Industrially, the application of this kind of techniques is made in four steps, which are the mechanical pre-treatment like polishing or any other mechanical surface processing, degreasing and cleaning the surface through the application of a hot alkaline or acid cleaner, polishing or electrobrightening. After the surface preparation, anodization is carried out. In which the part to be protected is placed as the anode in an electrolytic cell, and with the applying voltages, a stable oxides film will form on the anode surface. The mechanical, physical and chemical properties of such film will depend of the electrolyte, voltage and current applied, temperature and time of treatment. After the anodizing treatment, the part will be subjected to a post-treatment or dyeing and then sealing.

When this treatment is performed at low voltages, a thin protective oxides film is formed, usually accompanied with some water electrolysis. However, if the voltages are high, above the oxides layer breakdown potential, sparks will form on its surface, that will heat up the gases released by the substrate thus creating a plasma, those sparks will also induce pores on the oxides layer, creating a thick film with a porous structure i.e. a PEO film [27].

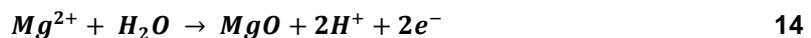
Usually, the typical PEO film structure is composed by three layers. A porous outer layer, called the "technology layer", which is formed by lower temperatures transformation phases. The intermediate interlayer, consisted by a denser oxide, is called the "functional layer" and is composed by phases formed due transformations at higher temperatures and pressures. And finally the "barrier layer", which is an interlayer formed between the functional layer and the substrate, even denser and thinner when compared to the functional layer.[28] And the enhanced corrosion protection, hardness and wear resistance given by the ceramic on the metal surface, is the result of the combined uniformity of electrolytic processes, with the local injection of high levels of energy [29].

4.3. Film formation

As it was previously said, a typical MAO film is composed by two main layers, a thin layer between the substrate and an outer loose porous layer. The reactions that will induce the film formation take place at the anode/electrolyte interface. The first step of the film formation consists in the dissolution of Mg from the substrate into Mg^{2+} , and release of oxygen due to the decomposition of OH^- ions and the oxidation of water [1, 2]. As it is simplified by the equations 11, 12, and 13 below:



After those reactions occur, it is time for reactions between the metal cations and electrolyte oxides to take place. First, due to the high applied potential, migration of metal cations outwards and electrolyte anions inwards will happen. The interactions between them, simplified in the equations 14, 15, below, will consist in the formation of metal oxides on the substrate by reactions with electrolyte species [27, 25]:



Other oxides will also be formed, but those will depend on the electrolyte composition, which will be explained later. The main dependence of the film structures is upon the current intensity and voltages applied, since all the migrations, in and outwards the substrates, are due to an applied potential.

The first layer to be formed is the inner one, the functional layer. This one is formed under low potentials, as in conventional anodization, and it will work as a barrier between the anode and the electrolyte thus increasing the potential applied needed for the film formation.

At this stage the film typically displays a fine porous structure and because of this insulating effect, the potential applied will increase with the coating's thickness, until it reaches a critical value called the breakdown potential, usually at a thinner part, in which this value is lower. When the potential applied reaches the breakdown potential of this oxides film, typically between 300 and 400 V, sparks across the surface form and heat the material, resulting in localized plasma reactions. Those sparks will melt the surrounding oxide, and the melt will escape through the discharge channels left by it. Due to the high cooling rates, the melt oxide solidifies just above the surface, thus closing the anodic film pores and forming a loose structure on top of it. Usually, in this second layer, which is thickest than the first one, there are several cracks on the surface due to thermal stresses induced by rapid cooling [28, 29]. The fact that this is a conversion coating technique [32], and the sintering interlocking, due to high temperatures and pressure imposed by the thermal stresses [33], resulting in the strong adhesion between the substrate and denser first layer and between this first layer and the porous outer layer.

4.4. Process Parameters

In MAO coatings, the current density, voltage applied, duty cycle, treatment time and pulse frequency and energy are found to be as important as the electrolyte composition and concentration since these parameters play a major role in thickness, composition, porosity and other defects, like cracks, in PEO films.

The most important of these factors is the pulse energy. This parameter has a vital influence in thickness, porosity, morphology and corrosion resistance of the coating. The increase in the pulse energy will increase the energy of the sparks across the surface, which will enlarge the discharge channels and providing more metal ions to react with electrolyte ions and thus increasing the coating thickness, however, the sparks energy increase and pores enlargement result in a more porous surface, diminishing the coating corrosion resistance [31]. The correlation between pulse energy and other parameters is given by the following formula in equation 16 [34].

$$E_p = \int_0^{t_p} U_p I_p dt \quad 16$$

E_p represents the pulse energy, that is explained above, t_p , the pulse-on time, U_p , the potential applied and I_p represents the current density.

As it was previously explained, with the oxide growing, the electrical conductivity decreases, therefore a higher voltage is needed for maintaining current density, thus, in a constant voltage regime, the current

will decrease with time and thickening of the oxides layer. So, since the current density is the main factor responsible for the sparking intensity and energy, keeping this parameter constant during a given time and duty cycle results in a thicker and looser coating than maintaining the voltage constant, consuming a smaller amount of time [35].

You et al. compared the corrosion resistance of plasma anodized ZK40 magnesium alloy with two different current densities, 3.5 and 9 A/dm², and concluded that in spite of being thicker, a larger current intensity can produce a coarser coating, thus diminishing the corrosion resistance of the coated samples [34].

The pulse on time and period ratio is called the duty cycle (dc). Increasing this parameter will increase the energy applied on the substrate during one period, which, in turn, will increase the plasma discharge energy and the size of the pores [31]. Having a higher energy on the plasma discharges, and therefore a larger amount of melt passing through the discharge channels, will enhance the adhesion between the coating and the substrate, through sintering interlocking, however, due to the thermal stresses induced by rapid solidification, more cracks over the surface will appear as it was reported by *Huan et al* [36], and, as the voltage increases, so does the energy of sparks across the surface, increasing the size of the pores, which will diminish the corrosion resistance of the coating. Therefore, an increase of the pulse off time gives time to the coating to heal such defects [37].

Several authors, like *Hussein et al.* [38] have studied the influence that the current mode and pulse timing have on PEO coatings morphology and corrosion behaviour. In this work, they have tested unipolar, bipolar and hybrid current modes on alkaline electrolytes. The unipolar samples revealed, as it was expected an interconnected porous structure, with the pores and cracks going all the way to the substrate, thus having the poorer corrosion resistance. The bipolar samples revealed more dense coatings due to the introduction of a cathodic component. This component will reduce the strong park discharges and provide longer off times between anodic pulses, which gives more time for the oxide to cool down, resulting in less porosity. However, a longer on time provides a longer sintering time, which can result in a denser layer [34, 35].

Usually, the experimental set up for plasma anodization, as seen in figure 5 consists in a few parts, those are the metal being coated, connected as the anode; the counter electrode, this can be the container itself, a piece of stainless steel in the solution, and is connected as a cathode; the refrigerator, that cools the solution; a stirrer; a high voltage AC power supply and a fume extraction vent [28].

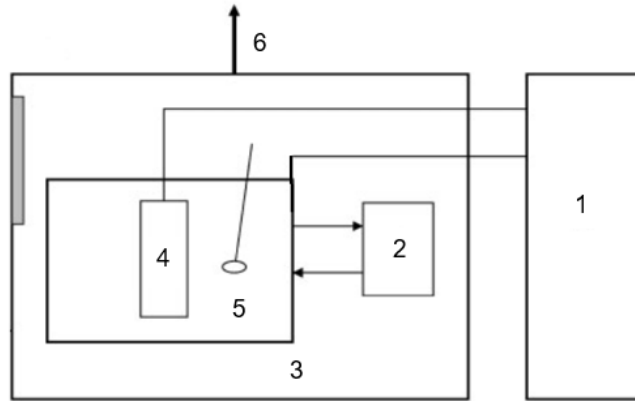


Figure 5 - Schematic representation of a PEO experimental set up. 1 – power supply; 2 – refrigerator; 3 – Container and counter electrode; 4 – working electrode; 5 – solution stirrer; 6 – Fume extraction vent. Adapted from [28].

4.4.1. Solution composition and concentration

The electrolyte composition and concentration are of vital importance for this kind of surface treatments since the coating formed on the anode surface will be directly, both in composition and morphology, affected by those.

The first requirement for the electrolyte is to provide a rapid metal passivation, since an insulating film on top of the substrate is vital for the entrance on the sparking regime. Secondly, it acts as a medium for enough electric energy transfer between the anode and cathode to induce oxidation of the metal surface. It is also an oxygen source to form metal oxides on the metal/electrolyte or oxide/electrolyte interface. And finally, the use of additives will provide the final coating with alloying elements that will enhance the corrosion and biocompatibility properties of the coating [17].

Usually, to prevent excessive metal dissolution, alkaline based electrolytes are used, however, due to their higher conductivity, voltages applied are lower and the coatings tend to have a coarser and more porous structure, which lowers the corrosion resistance [39], and if the coating gets to thick, it cannot be broken by the spark discharges, which restrains the PEO process [40]. If the pH of a given electrolyte is too low, then it won't provide enough conditions for the discharge sparks to happen, and instead, excessive metal dissolution would occur and a great part of the energy imposed would be transformed in thermal energy, resulting in a quick rising of the electrolyte temperature [40]. Therefore, the pH of an acidic electrolyte should be between 3 and 6, and for an alkaline electrolyte, it should be between 8 and 13 [37].

The concentration of the electrolyte also plays a vital role on this equation. It has a direct influence on the electrolyte's conductivity and heat capacity. *R. Zhang et al.* [41] reached the conclusion that an increase in the phytic acid concentration will obviously increase the phosphorous content in the coating and decrease the electrolyte's conductivity, which, in turn, will increase the breakdown potential. The influence of sodium aluminate and potassium fluoride on the solution conductivity was studied by *H. Guo et al.* [42], the results showed no variation of the electrolytes conductivity with the increasing of the

first one concentration. On the other hand, the increasing concentration of KF showed an increase on the solution conductivity, which increased the rate of deposition and decreased the breakdown voltage. As it was previously explained, Ohm's law states that the potential applied is proportional to the current having the resistance as proportionality constant. And the Joule heating effect consists in the heating produced by a material or media due to its resistivity and time of applied potential. Both phenomena mentioned above can be described by the following equation, in which J represents the energy wasted in temperature increase (Joule), I is the current density (Ampere), R is the material resistivity (ohm) and t is the treatment time (second).

$$J = I^2 R t$$

17

Rearranging the equation above with Ohm's law, one can easily see that increasing the solution's resistivity, the temperature will also increase. And since the electrolyte conductivity is proportional to its concentration, the joule heating effect will decrease with the electrolyte concentration.

Several additives can be added to the solution to increase certain coating properties, such as hardness, biocompatibility, homogeneity, corrosion resistance and so on, and to change some electrolyte properties, like conductivity, heat capacity among others [31].

4.5. Hydrothermal treatment

Hydrothermal deposition is one of the simplest and cost-effective techniques for the deposition of coatings on metallic materials. It consists in dipping the material in a heated solution, for a certain period of time. Usually, this treatment is performed at temperatures above 80°C, and for periods longer than 1.5 hours [43].

The pH of the solution is also of main importance, since magnesium, according to its E-pH diagram in figure 1, corrodes at pH lower than 11, and Mg ions substitute Ca on hydroxyapatite's structure, preventing its crystallization. However, some authors suggest that the corrosion resistance of Hap coatings is higher when the treatment is made at a pH of 7.3, which is close to the human body [44]. Hence the need of a pre-treatment, like plasma anodization, for the magnesium.

As in plasma anodization, hydrothermal treatments also produce a coating with a denser inner layer, and a coarser outer one, however this is more evident with an increasing treatment time. Due to the previously explained alkalisation of the solution close to the magnesium surface, as we can see in figure 6, 1 and 2, a $Mg(OH)_2$ -layer forms on the surface, after that, a dome shaped Hap layer precipitates on the surface consisting of textured HAp crystals, oriented parallel to the surface, on top of a dense layer of randomly oriented HAp crystals. Then, with prolonged treatment time, rod-like Hap structures form on top of the dome shaped layer, and all the different parts of the coating tend to grow with time [45]. However, when this treatment is performed on top of a bare metal, like in the case of figure 6, the

appearance of the metal/Mg(OH)₂ and Mg(OH)₂/HAp interfaces, diminishes the bonding properties between the metal and the coating, decreasing the coating's effectiveness in the corrosion protection.

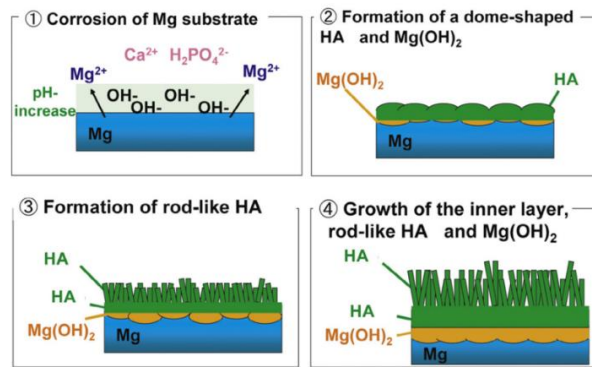


Figure 6 - Growth mechanism of HAp coatings with hydrothermal treatments on bare Mg [45].

5. Characterization techniques

5.1. Electrochemical Impedance Spectroscopy

One of the most used techniques to evaluate the corrosion behaviour of materials, especially in electrolytes of low conductivity, is the electrochemical impedance spectroscopy (EIS). This technique is based on the imposition of a small alternating potential, recording an alternating response, like in DC methods, AC techniques also follow Ohm's law, however, as it can be seen in equation 18, because the potential applied is frequency dependent, the current will be as well.

$$Z(\omega) = \frac{V(\omega)}{I(\omega)} \quad 18$$

$$V(\omega) = V_0 \sin(\omega t) \quad 19$$

$$I(\omega) = I_0 \sin(\omega t + \theta) \quad 20$$

The potential applied, V , is a sinusoidal wave, like the one in equation 19, and the response current, I , therefore, will be also a sinusoidal wave, however out of phase by an amount θ , like in equation 20. The displacement of phases between the input potential and the output current happens because there is charge relaxation time a lag between the applied voltage and the current response.

Usually, the potential is applied over a range of frequencies, typically between 0.1Hz and 100 kHz. The impedance of an electrode is the proportionality factor to an alternating applied potential, and the response current.

According to Euler's relationship, because both the potential and response current are sinusoidal waves, impedance can be plotted on the complex plane, meaning that it will have a real part, that measures the resistance, and an imaginary one, measuring the capacitance. Impedance are shown graphically on a Nyquist diagram, like in figure 7. The diagram's shape, together with the data collected in the Bode plots of figure 8, provide detailed information about the electrochemical behaviour of a system, being possible, then, to modulate an equivalent circuit, like the one on the upper left corner of figure 7, and derivate all the values relevant to the corrosion behaviour like the charge transfer resistance, double-layer capacitance, and so on.

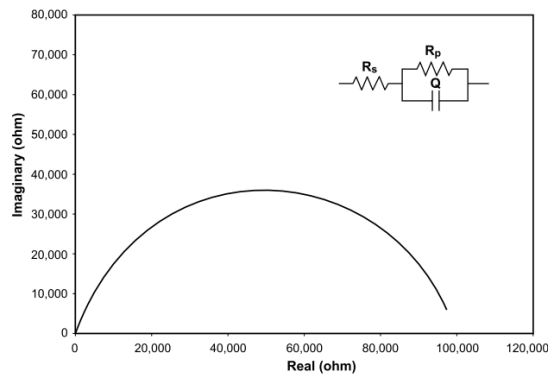


Figure 7 - Example of a Nyquist plot.[13]

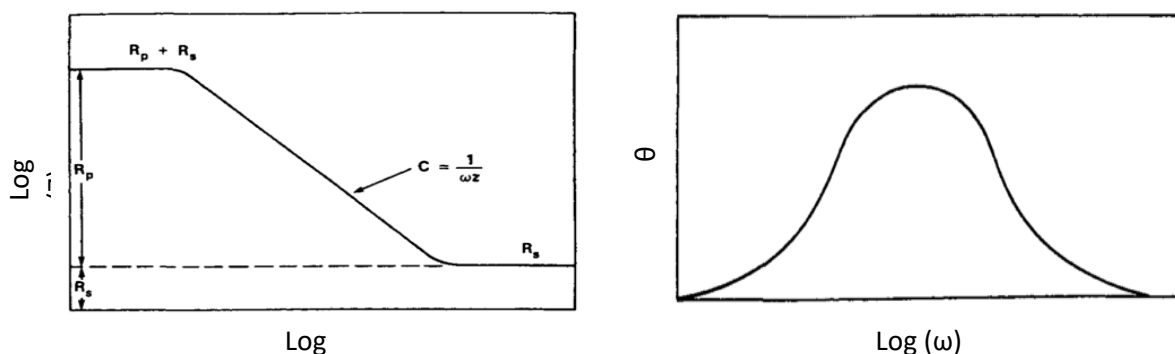


Figure 8 – Example of Bode (left) and phase angle plots (right). Adapted from. [18]

EIS measurements are usually made with the help of potentiostats. As seen in figure 9, a potentiostat for EIS consists in an operational amplifier, which maintains the reference electrode connected to its inverted input at held potential V_{set} by current imposed by the counter electrode. Maintaining a constant potential difference between the reference electrode (V_{set}) and the working electrode which is at a virtual ground potential (V_{ground}). In potentiostats specific for EIS measurements, a voltage adder imposes an AC voltage on top of the DC voltage, imposed on the WE by a frequency function analyser. The response current will be measured by a current follower [46].

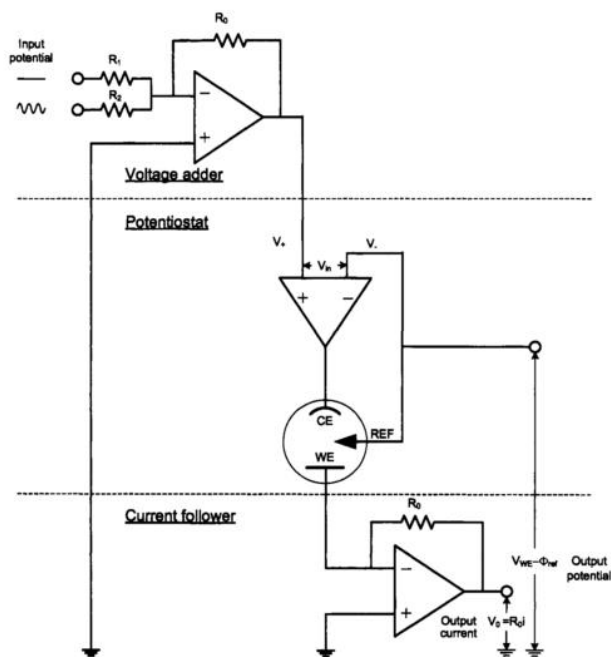


Figure 9 - Schematic representation of a potentiostat working principles [46].

This technique is best suited to study the interfacial reactions of a corroding electrode, properties of coated metals and passive films. Since their electrochemical behaviour is more complex than in bare metals, and, in most of the cases, both Nyquist and Bode plots have much more complex shapes, a number of circuits elements were proposed, like resistors, capacitors, inductors, among others [22, 23]. Most of the times there is a connection between the real behaviour of a given system and the modulation of a series of discrete elements on an electric circuit like the one inserted in figure 7.

In an electrolytic cell, the electrolyte is assumed to behave as a perfect resistor, see table 4, hence it will only contribute to the real part on the overall impedance. On the electrode surface, several reactions can happen, due to the accumulation of charges on its surface, the adsorption of species and so on. The accumulation of charges due to an applied potential will be measured by the capacitance of the material, and the relaxation time of the species present will give rise to the phase displacement, given in the phase angle plot. Because the current is given by the derivate of the electric charge, q , over time, equation 21 relates the current, I , with the capacitance, C .

$$I = C \frac{dq}{dt}$$

21

Table 4 - Impedance of common equivalent circuits. Adapted from [47].

Resistor	$R = \frac{V}{I}$	$Z_R = R$
Capacitor	$I(\omega) = C \frac{dV(\omega)}{d(t)}$	$Z_C = \frac{1}{j\omega C}$
Inductor	$V(\omega) = L \frac{dI(\omega)}{dt}$	$Z_L = j\omega L$
Constant phase element	-	$Z_{cpe} = \frac{1}{(j\omega)^p C}$

The impedance of an inductor is directly proportional to the frequency and inductance, however there are some doubts about its physical meaning, so negative capacitors are used instead sometimes.

The capacitor element, most of the times, doesn't take into account the surface inhomogeneities, presence of adsorbed species and non-uniform current distribution, assuming that the capacitance of real systems always behave like a perfect capacitor. A constant phase element is a capacitor with the frequency applied elevated to an exponent P , between 0 and 1, that takes those factors into account approximating the modelled capacitance from the real one [49].

The overall impedance of a system will be the sum of all the discrete elements that compose the equivalent circuit. The impedance of the equivalent circuit on figure 7, for example, will be the sum of Z_1 , which will be equal to R_s , and Z_2 , that will result from the next equation.

$$\frac{1}{Z_2} = \frac{1}{Z_3} + \frac{1}{Z_4} \quad 22$$

Being Z_3 and Z_4 the impedances associated with R_s and Q respectively [46].

In this work, EIS was chosen instead of any DC method, because with EIS is possible apply very small amplitude signals, avoiding changes in the sample surface, induced by the time dependent DC methods, as explained before [13].

5.2. Scanning Electron Microscopy

Scanning electron microscopy is a type of instrument used to obtain information about the crystallographic structure, chemical composition and other properties of a sample, through magnified images of a specimen. The modern SEM instrument was invented by the Professor Sir Charles Oatley during the 50s/60s, at the University of Cambridge.

Figure 10 shows a schematic illustration of the working principles of a SEM instrument. First, a beam of electrons is emitted by a thermionic, Schottky or field emission cathode, this electrons beam will be accelerated by a voltage difference imposed by an anode. After that, a series of apertures, electromagnetic lenses and coils will decrease the electron beam diameter from 10 – 50 μm , for thermionic, or 10 – 100 nm, for Schottky or field emission guns, until a beam with a diameter of 1 – 20 nm. Finally, a deflection coil system points the electron beam across sample surface, scanning it in raster pattern, in close spaced discrete locations [47, 48].

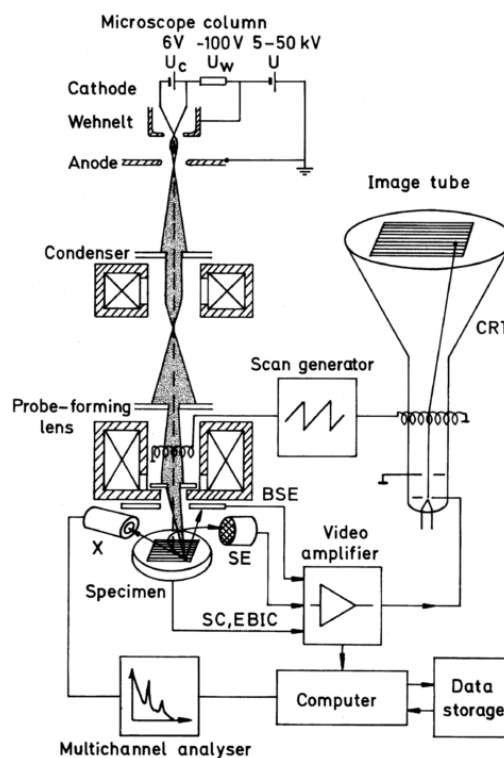


Figure 10 - Schematic representation of the SEM principles [50].

After this primary beam of electrons (PE) hits the sample, part of the electrons is deflected and scattered by the electric fields of the sample's atoms, those backscattered electrons (BSE) maintain a large fraction of their initial energy, and because of their high kinetic energy, their trajectory cannot be changed without influencing the primary beam. Therefore, the BSE detector is concentrated with the last electromagnetic lens. If the electron beam energy is high enough, part of its kinetic energy can be

absorbed by the structure, ionizing an atom that when returning to its original state can release a x-ray photon. If this photon, before leaving the sample, hits another atom, an electron can be expelled, being this electron define as an Auger electron (AE).

Another part of the PE, depending on the target density, chemical composition and the beam energy, penetrates the sample, reaching a depth of $10\mu\text{m} - 10\text{nm}$, increasing the energy state of its atoms, and, therefore, expelling its electrons. Due to the energy absorption, this secondary electrons (SE) are ejected from the sample with low kinetic energy, typically between 0-5 eV but their energy can go up to 50 eV, above which they are considered BSE or AE [47, 48].

Due to their low energy, AE and SE only can escape the sample if they are at least a few nanometres close to the surface, and because of the same reason, they are highly susceptible to a change in trajectory through a positively biased collector grid, and after accelerated towards a, also positively biased, scintillator. The primary electron beam is coupled with a separated cathode ray tube (CRT), and the intensity that the detectors receive the BSE, SE and AE, will be proportional to the intensity of the electron beam of the CRT, thus forming an image in a grayscale [50].

When a X ray photon is produced by the returning of an atom to its ground state of ionization, it will end up on a Silicon single crystal with Lithium atoms drifted (or diffused) from one end to another, turning the single crystal in p-i-n type diode. After the p side of the crystal gets ionized by the x ray that comes from the sample, an electron-hole pair is produced, being the total charge produced obviously proportional to the x-ray energy emitted by the sample. This charge produced on the crystal is amplified and read and presented on the CRT display. Since each element has its own energy signature, EDS analysis gives us detailed information about the chemical composition and distribution of a material [52].

5.3. X-ray Diffraction Spectroscopy

X-Ray Diffraction (XRD), is one of the most used techniques for materials characterization in the world. By shooting X-rays on a specific angle, θ , towards a crystalline material, as in figure 11 and an elastic scattering happens, the diffracted waves will still be in phase with the incident ones and retain their original energy. Due to the periodic nature of crystalline planes, constructive interference will occur between waves that were diffracted by the same plane, thus creating a diffraction patter.

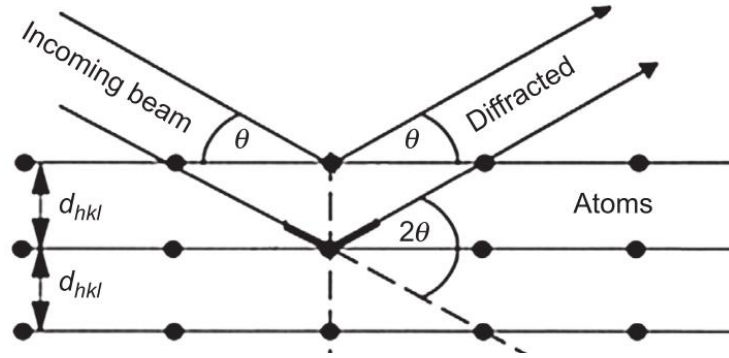


Figure 11 - Schematic representation of Bragg's law. [53]

According to Bragg's law, equation 23, the distance between crystallographic planes can be obtained. In which n is the diffraction number, λ is the incident x-ray wave length and θ is the incident angle.

$$n\lambda = 2d_{hkl}\sin(\theta) \quad 23$$

The sum of the radiation intensity diffracted by each atom on a crystallographic plane (I_{hkl}) is proportional to the square of structure factor. Equation 24 explains the relationship between the intensity diffracted and the structure factor (F) and the equation 25 relates the complex number F with the miller indices of a plane and cartesian coordinates of a unit cell.

$$I_{hkl} = K|F_{hkl}|^2 (f_a e^{-B\sin^2(\theta)/\lambda^2}) A \times L(\theta) \times P(\theta) \times m \quad 24$$

$$F_{hkl} = \sum_{j=1}^N f_j \times e^{2\pi i(hx_j + ky_j + lz_j)} \quad 25$$

In the first relation, A is the absorption factor, L is the Lorentz factor, P is the Polarization factor and m is the multiplicity of planes, meaning, the amount of planes that can diffract a specific Bragg angle, $f_a \exp(-B\sin^2(\theta)/\lambda^2)$ takes into account the thermal displacement of atoms, and K is a constant independent of the temperature [53].

Further investigation on these constants is outside the scope of this work.

However, real materials have imperfections, defects and so on, therefore the pattern detected would be altered, therefore one needs to consider several aspects that can influence the results.

Instrumental broadening, composition heterogeneity, the size of crystallites, or coherently diffracted regions, crystallographic defects and structure strains will contribute for the peak broadening. Based on the peak position, one can obtain qualitative information of phase analysis, chemical composition, lattice parameters space group and macro stresses. The peak intensity provides data on the crystal structure, (occupancy, atomic positions and so on) and texture.

6. Materials and methods

6.1. Plasma Electrolytic oxidation

The samples used in this treatment were cut from a wrought magnesium AZ31 rod. The nominal composition is listed on table 5. This alloy was chosen due to its low content in toxic elements, such as aluminium, and superior mechanical properties when compared to other Mg alloys.

Table 5 - Nominal composition of AZ31 wrought alloy. Adapted from [54].

Element	Al	Zn	Si	Cu	Fe	Ni	Mn	Other
Content (wt%)	2.5 – 3.5	0.5 – 1.5	0.1	0.1	0.03	0.005	0.05 – 0.4	0.1

Figure 12 shows a sample used before treatment. The exposed area was 2.25cm². A copper wire was glued on one side with high purity silver paint of SPI®. The sample was imbedded in epoxy resin to isolate the wire/AZ31 junction from the solution.

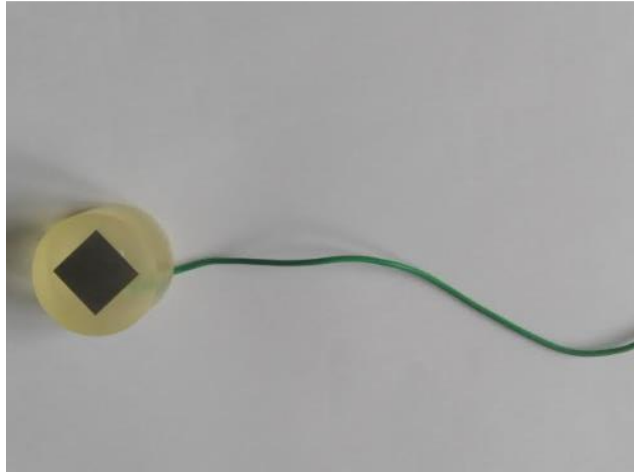


Figure 12 - Samples used before treatment.

Before the anodization, all samples were polished with SiC emery paper of 400, 800, 1000 and 2500, cleaned with alcohol and dried in air.

The apparatus used for the treatment, showed in figure 13, involved an Agilent® 6813B AC power source, with the maximum power of 1750 VA. The cell consisted in a laboratory glass beaker of 1L and the solution temperature was kept at $10 \pm 0.5^\circ\text{C}$ by using a Julabo® refrigerator that kept a cooling oil flowing through a 316 stainless-steel tubular spring. The specimens were connected to the positive pole, as an anode, and the cathode was the SS 316 spring.



Figure 13 -Experimental set up for the PEO treatment.

The solutions chemical composition is displayed in table 6, these solutions were chosen because all the elements can be used for bone growth, and literature suggests that oxides from those compounds have a very high corrosion resistance and biocompatibility due to its chemical composition being close to the

human bone. In total, four solutions were tested, differing in composition and concentration. An approximate volume of 500 mL of solution was used at each time.

Table 6 - Solutions used in the MAO treatment

	Na_3PO_4 (g/L)	KOH (g/L)	$\text{Ca}(\text{OH})_2$ (g/L)
Solution 1	10	2	-
Solution 2	20	4	-
Solution 3	10	-	2
Solution 4	20	-	2

The treatment itself was performed with current control, offering a better adhesion and more cohesion to the coatings. The duty cycle of all the anodizations was 20% and the frequency was 100Hz. Two different programs were used with times and currents shown in table 7. Both treatment programs were tested in all the solutions to evaluate the current density, composition, concentration and treatment time effects in morphology, thickness, porosity, corrosion resistance and HAp forming ability.

Table 7 - Plasma electrolytic oxidation programs.

	Current density (A/cm^2)	Time (s)
Program A	0.08	900
Program B	0.25	600

Table 8 displays an overall view of the conditions in which all samples were coated before the hydrothermal treatment.

Table 8 – Overall view of the Plasma Electrolytic Anodization for all samples.

Sample Designation

	1A	1B	2A	2B	3A	3B	4A	4B	
Solution (g/L)	Na ₃ PO ₄	10	10	20	20	10	10	20	20
	KOH	2	2	4	4	-	-	-	-
	Ca(OH) ₂	-	-	-	-	2	2	2	2
I (A/cm ²)	0.08	0.25	0.08	0.25	0.08	0.25	0.08	0.25	
V _{max} (V)	340	421	292	382	354	421	299	411	

6.2. Hydrothermal treatment

The hydrothermal treatment of the PEO coating used the set up shown in figure 14. The solution temperature was kept at $90 \pm 0.5^\circ\text{C}$, and the container had 100mL of solution.



Figure 14 - Experimental hydrothermal treatment set up.

The heater was the same equipment used as a cooler in the PEO treatment. The treatment times, solutions and pH used are displayed on the table 9. NaOH was added to all solutions until the pH reach the desired value.

The treatment was tested on the two PEO samples that showed the higher corrosion resistance, and both were kept in solution for 4 hours.

Table 9 - Experimental conditions of the HT treatments

	KH_2PO_4 (mol L ⁻¹)	EDTA (Ca) (mol L ⁻¹)	pH	Time (h)
HT1	0.1	0.1	9.5	4
HT2	0.1	0.1	8.5	4

6.3. Thickness measurement

The thickness was measured with a thickness coating gauge from Elcometer®. In order to evaluate the composition, concentration and current density influence on the coating thickness and avoid errors due to local inhomogeneities, three measurements were made on the surface of each sample.

6.4. Electrochemical Impedance spectroscopy

In this work all the impedance spectra were performed with a Gamry® Reference 600 Plus, and the software was Gamry Framework, at open circuit potential, versus a calomel reference electrode and a platinum counter electrode. The starting frequency was 10⁵Hz and the final was 0.01, with 9 points per decade.

The electrolyte used in the first round of impedances was a solution of 0.1M NaCl, inside a faraday cage, at 25°C, and the working electrode had an exposed area of 2.25 cm².

The second round was performed inside a Memmert® HPP260 oven, keeping the temperature at 37°C and the electrolyte used was Simulated Body Fluids, SBF, with the composition in table 11. The working electrodes exposed areas is listed in table 10, due to the need of sealing the interface between the working area and the epoxy resin, with epoxy glue.

Table 10 - Working electrodes exposed areas on the 2^o round of impedances.

	2B	4B	2BHt₁	2BHt₂	4BHt₁	4BHt₂
Surface area (cm²)	0.8	1.32	0.5	1.21	1.56	1.44

SBF is a solution used to simulate the physiological environment by having the same pH and ionic composition of human blood plasma. Several works have proven that this solution is efficient in predicting, *in vitro*, if a material will or not bond with living bone and withstand the electrochemical conditions for enough time. The ability to form apatite immersed in SBF has been proven to be proportional to the ability to induce growing and bond with living bone [55].

Table 11 - Comparison of ionic charges of SBF and human blood plasma. Adapted from [55].

	Ion concentration (mM)							
	Na⁺	K⁺	Mg²⁺	Ca²⁺	Cl⁻	HCO₃⁻	HPO₄²⁻	SO₄²⁻
Human								
Blood	142.0	5.0	1.5	2.5	103.0	27.0	1.0	0.5
Plasma								
SBF	142.0	5.0	1.5	2.5	147.8	4.2	1.0	0.5

6.5. Scanning Electron Microscopy

The surface morphology was evaluated with a Hitachi® S2400 analytical SEM, equipped with a Bruker® light elements EDS detector, that was used to obtain information about the chemical composition of the PEO coatings before and after the hydrothermal treatment and SBF immersion. All PEO coated samples were coated with gold, to avoid charging effects typical from insulating materials. The samples after the hydrothermal treatment and the SBF immersion were coated with chromium.

6.6. X – ray diffraction

In this work, all the XRD measurements made were with a Philips PW diffractometer, the radiation used was $\text{CuK}\alpha$, with a wave length of 1.5842\AA , with a power of 30W and 40mA, an increment of 0.01° , with a rate of one step per second. The measurement took place in the range of $10^\circ - 20^\circ$ in a continuous mode. All the diffraction patterns obtained were compared with patterns present both in the software Match® and the free online database RRUFF.

7. Results

7.1. Thickness measurement

Table 12 lists the average thicknesses obtained with the plasma electrolytic anodization and in table 13 is displayed the average thickness of all hydrothermally treated samples before and after the immersion in SBF.

Table 12 - Average thickness obtained for anodized samples.

Sample	1A	1B	2A	2B	3A	3B	4A	4B
Thickness (μm)	14.5	28.4	19.4	49.2	12.5	22.6	20.2	43.2

Table 13 - Average thicknesses obtained for samples 2B and 4B after three days of SBF immersion, and of hydrothermally treated samples. Before and after SBF immersion.

Sample	2B SBF	4B SBF	2BHt ₁	2BHt ₁ SBF	2BHt ₂	2BHt ₂ SBF	4BHt ₁	4BHt ₁ SBF	4BHt ₂	4BHt ₂ SBF
Thickness (μm)	45.3	48.5	51.6	52.1	51.3	53.2	47.9	49.4	47.5	51.8

As expected from literature, the thickness of the PEO coatings increased both with the solution composition and the current intensity. After the hydrothermal treatments, sample 2B didn't present a big increase in thickness, on both treatments, increasing approximately $2\mu\text{m}$, and the sample 4B thickness increase was about $4\mu\text{m}$, also on both treatments. Those results suggest that one value of pH on the hydrothermal treatments has no influence on the coatings thickness. Samples 2B and 4B increased in thickness, meaning that the SBF immersion induced the deposition of electrolyte species on the sample surface.

7.2. Morphology and microstructure

Figures 15 to 22 show SEM images taken from samples surface after the respective PEO treatment. Comparing samples, A and B, treated with the same solution, 1, 2, 3 or 4, in all cases the samples treated with program A display a more uniform distribution of small pores than samples treated with the program B due to the lower voltages achieved in the end of the treatment. The higher voltages achieved on coatings produced with program B promote sparks of longer duration and a larger size, meaning that the amount of oxide melt and formed on the surface will be larger. Hence the lower pore density and the higher pore diameter of samples B. After the breakdown potential, several sparks form on the coating's surface, leading to a local high temperature, which melts the oxide and the metal beneath it creating discharge channels. The high pressure to which the molten metal is subjected expels it through the discharge channel formed on the oxides layer by the spark. The molten metal, then, reacts with the electrolyte, and the rapid solidification creates several thermal constrains leading to formation of several cracks on all the coatings surface. The size of the sparks is proportional to the pulse energy, which is proportional to the current intensity applied, hence the samples subjected to 0.25 A/cm^2 have a larger pore diameter than the ones subjected to 0.08 A/cm^2 .

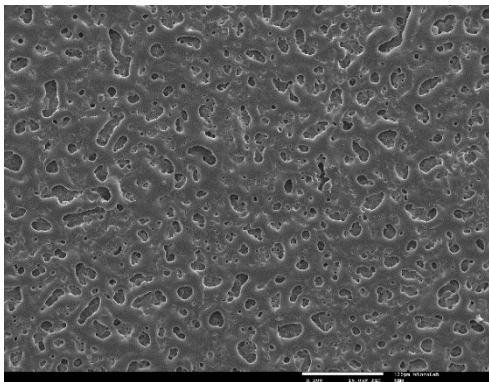


Figure 15 - SEM micrograph of sample 1A 200x.

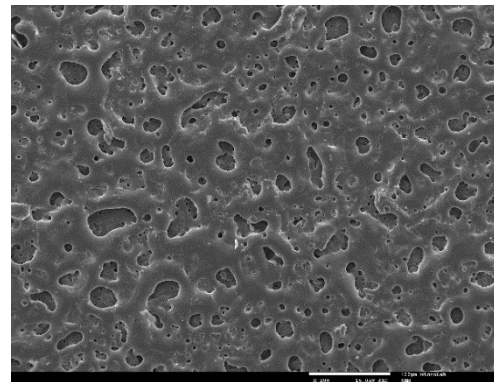


Figure 16 - SEM micrograph of sample 1B 200x.

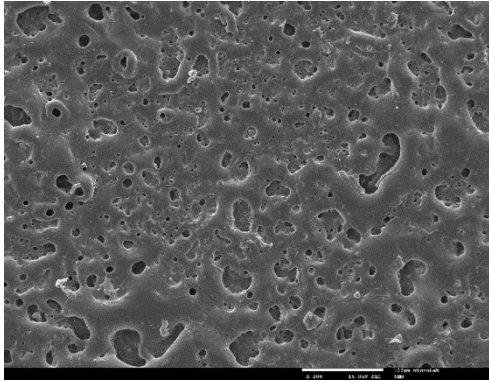


Figure 17 - SEM micrograph of sample 2A 200x.

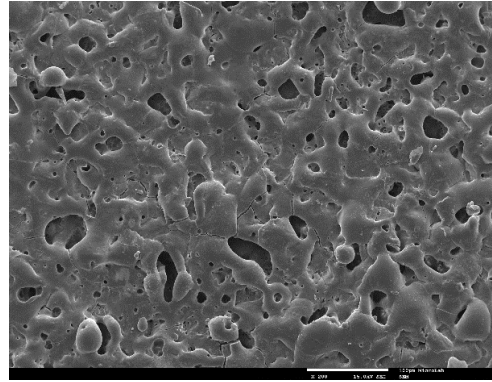


Figure 18 - SEM micrograph of sample 2B 200x.

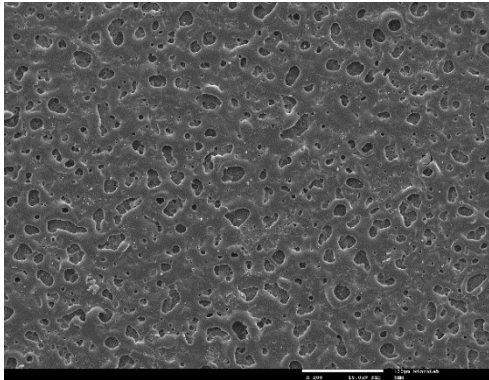


Figure 19 - SEM micrograph of sample 3A 200x.

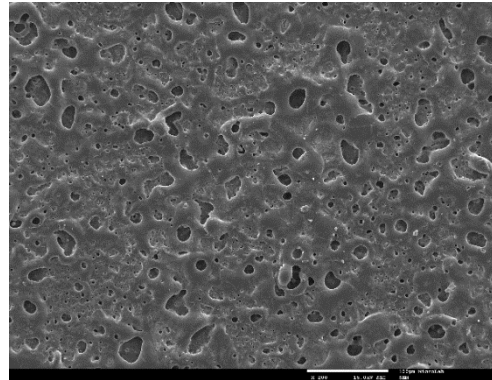


Figure 20 - SEM micrograph of sample 3B 200x.

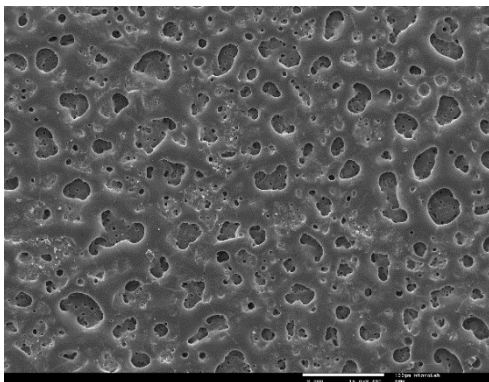


Figure 21 - SEM micrograph of sample 4A 200x.

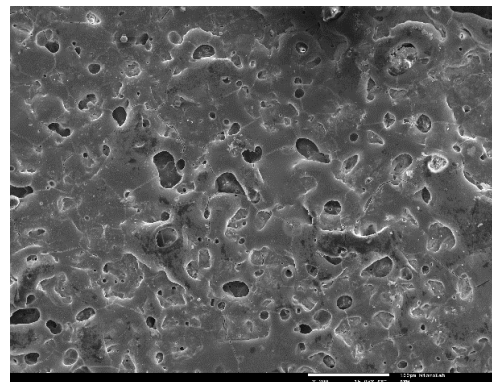


Figure 22 - SEM micrograph of sample 4B 200x.

The results of the EDS analysis performed on all coated samples is presented in table 14. Apart from samples 4A, that showed a smaller amount of phosphorous, and sample 1B, that showed a smaller

amount of potassium, the atomic percentages of each element is relatively similar in all samples, meaning that the coatings are composed mainly of magnesium oxides/hydroxides and phosphates.

Table 14 - Atomic percentages of all PEO coatings.

	1A	1B	2A	2B	3A	3B	4A	4B
Mg (At%)	22.3	20.0	23.3	21.0	24.5	16.7	15.0	15.2
O (At%)	60.4	59.6	49.5	56.3	52.9	60.3	60.3	61.1
Na (At%)	1.5	2.5	2.2	1.4	1.5	1.8	2.6	2.3
P (At%)	15.8	16.3	16.0	19.5	17.3	15.1	8.2	15.9
K (At%)	0	1.8	8.7	1.8	-	-	-	-
Zn (At%)	0	0	0	0.1	0	0	0	0
Al (At%)	0	0	0	0	0	0	0	0.2
Ca (At%)	-	-	-	-	3.7	6.2	6.3	5.3

Figures 23 to 30 display SEM micrographs of samples 2B and 4B after the hydrothermal treatments 1 and 2. Comparing samples 2BHt₁ in figure 23 and 2BHt₂ in figure 25 with sample 2B (figure 18), one can see that the pore diameter decreased, indicating that pores were sealed by the treatment. Figures 24 and 26 show the sample 2BHt₁ and 2BHt₂ in a 5000x magnification. Needle-like structures grew on the entire surface, suggesting the nucleation of calcium phosphates, and, according to table 15, the ratio between calcium and phosphorus is close to 1.6, suggesting that this needle-like structure on the sample surface is in fact hydroxyapatite.

Sample 4BHt₁ and 4BHt₂, in figures 27 and 29, also display a surface with a lower pore diameter than sample 4B in figure 22, indicating that also in this case the hydrothermal treatment has led to a decrease in pores size, and one can also see the growth of needle-like calcium phosphates on sample 4BHt₁, however, in sample 4BHt₂, this needle like structure is absent, suggesting that in this case, the nucleation rate of HAp crystals is much higher, leading to a more amorphous microstructure, as seen in figure 30.

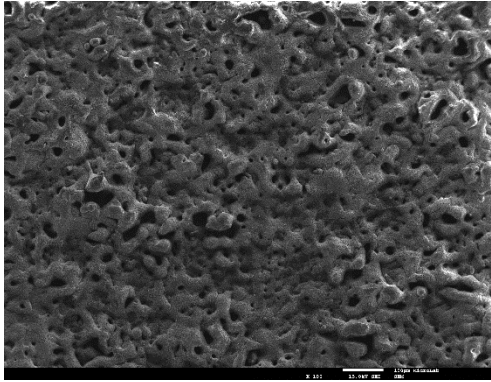


Figure 23 – SEM micrograph of sample 2BHt₁ 100x.

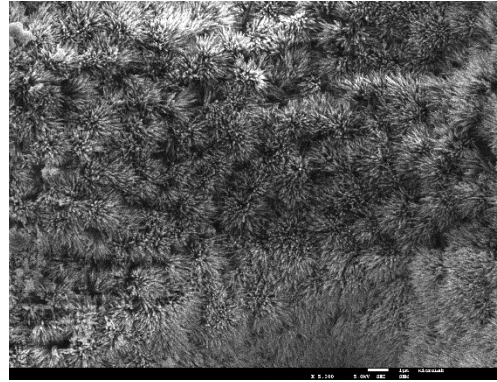


Figure 24 - SEM micrograph of sample 2BHt₁ 5000x.

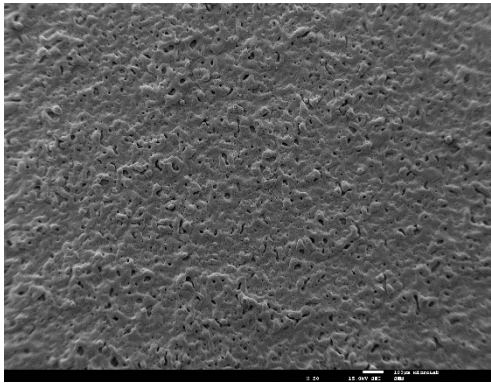


Figure 25 - SEM micrograph of sample 2BHt₂ 50x.

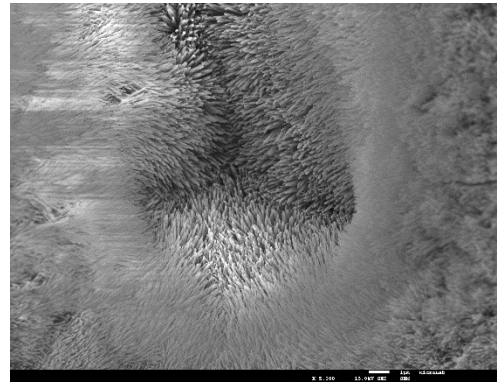


Figure 26 - SEM micrograph of sample 2BHt₂ 5000x

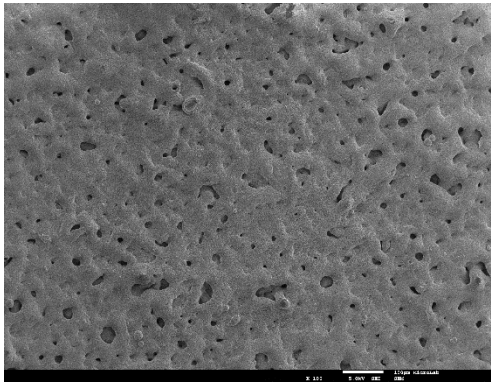


Figure 27 - SEM micrograph of sample 4BHt₁ 100x.

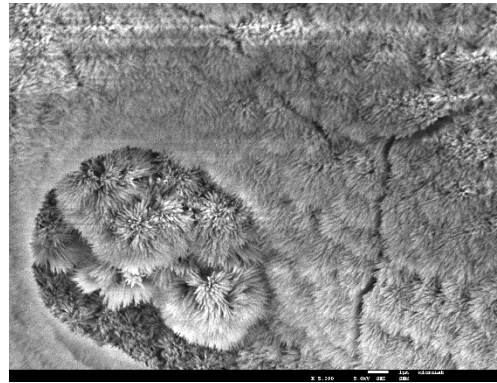


Figure 28 - SEM micrograph of sample 4BHt₁ 5000x.

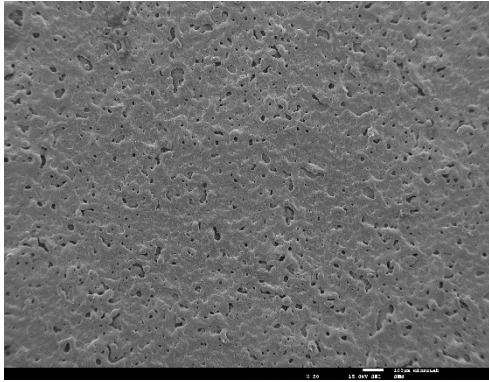


Figure 29 - SEM micrograph of sample 4BHt₂ 50x.

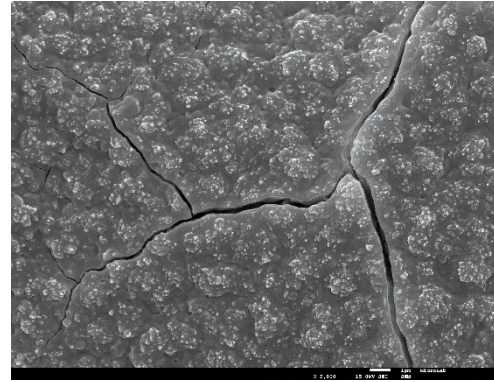


Figure 30 - SEM micrograph of sample 4BHt₂ 5000x.

Table 15 - EDS results of hydrothermally treated samples

	2BHt ₁	2BHt ₂	4BHt ₁	4BHt ₂
Mg (At%)	0.4	0.6	0.5	0.6
O (At%)	58.7	50.5	58.3	52.4
Na (At%)	0.6	0.5	0.7	1.4
P (At%)	13.9	16.5	14.2	15.5
K (At%)	0.3	0.6	0	1.9
Ca (At%)	22.6	27.4	23.8	23.0
Ca/P Ratio	1.6	1.7	1.7	1.5

Figure 31 displays the XRD patterns of all hydrothermally treated samples and, for comparison, the bare alloy. All the patterns present the α -magnesium phase, however the γ -Mg₁₇Al₁₂ phase, expected according to Mg-Al phase diagram, is not seen in the bare alloy spectrogram, probably due to its low amount, and traces of magnesium oxide were found, which was expected since magnesium is a reactive metal [56].

All curves of the hydrothermally treated samples present very similar structures, as expected from SEM micrographs and EDS results, Some MgO phase was found, and some peaks of HAp were found between 20.5, approximately, and 30 degrees.

In the case of sample 4BHt₂, the XRD pattern showed a larger presence of an amorphous phase on the 2θ below 32°. As seen in figure 30, the sample's micrograph also shows an amorphous structure.

The most intense peaks observed belong to the α -Mg phase due to this coating being very thin compared to the substrate.

It is important to refer that several calcium and magnesium phosphates standard patterns could fit in the diagrams bellow, due to the coatings being too thin for a normal XRD effective analysis, meaning that the peaks observed are probably Hap peaks, however one can not affirm that the coating is entirely made of Hap and MgO.

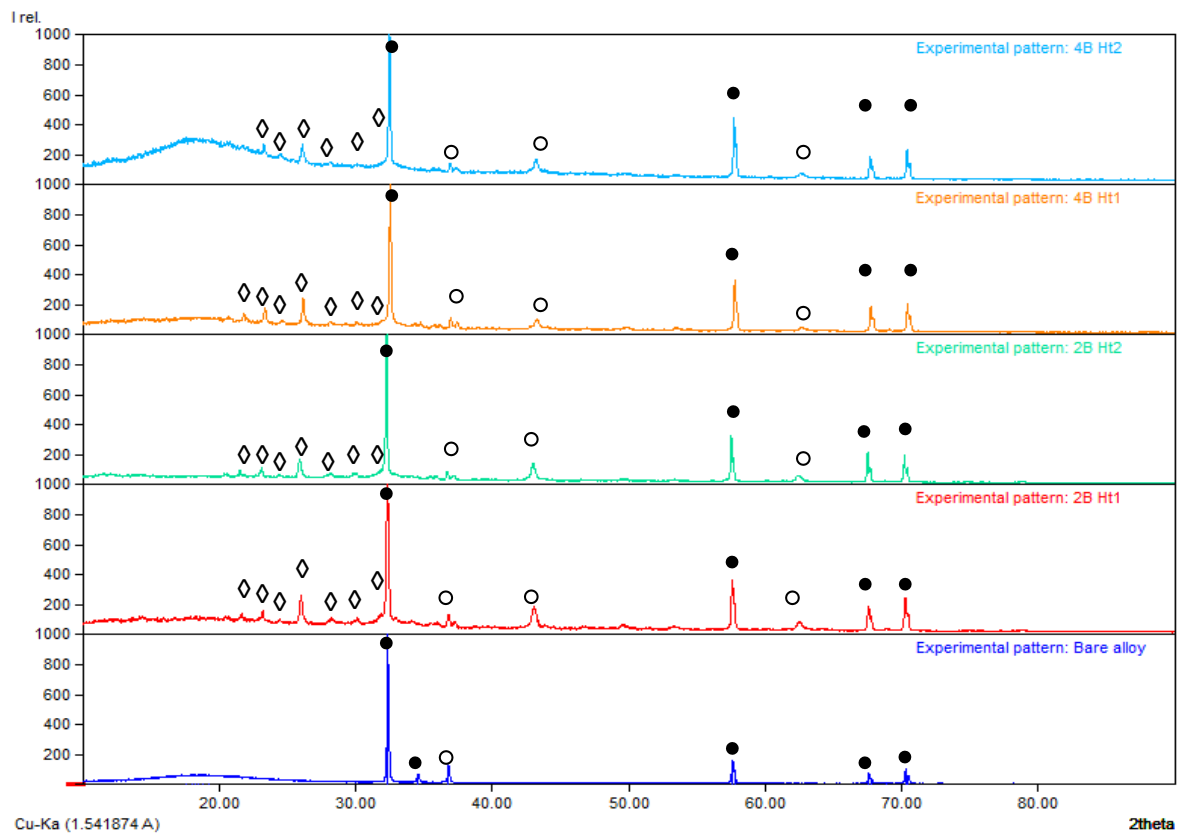


Figure 31 - XRD patterns of bare alloy and Ht samples before the immersion test. \diamond - HAp; \bullet - α -Mg; \circ - MgO.

The SEM micrographs of the samples 2BH₂ and 4BH₁ after the hydrothermal treatment are displayed in figures 32 and 33, both samples present very similar structures, suggesting that neither the MAO coating composition nor the pH difference (Δ pH=1) between the Ht solutions, do not seem to have a vital influence on the growing of hydroxyapatite on the samples surface.

The EDS results, seen in table 16, show the presence of only calcium, phosphorous and potassium on the samples surface, suggesting magnesium had almost no intervention in the formation of the outer surface phosphate layer.

The structure observed on both samples is a worm-like hydroxyapatite, which is corroborated by the EDS results for the same samples, and suggested by similar previous work [57].

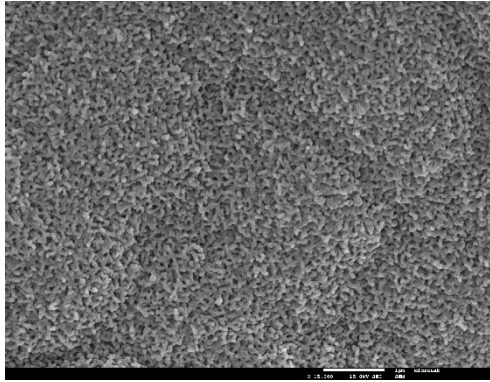


Figure 32 – 2BHt₂ after 72 h of SBF immersion.

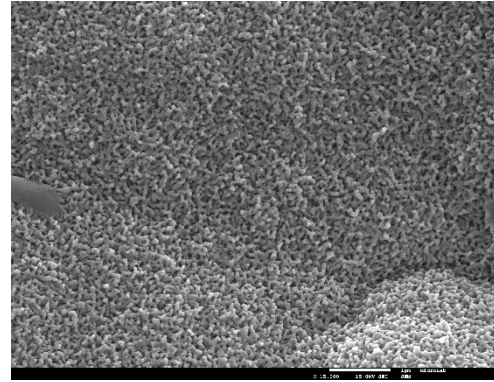


Figure 33 - 4BHt₁ after 72h of SBF immersion

Table 16 - EDS results for samples after immersion in SBF.

	2BHt ₁ SBF	4BHt ₂ SBF
P (At%)	21.9	20.9
O (At%)	37.8	42.9
Ca (At%)	40.3	36.3
Ca/P Ratio	1.8	1.7

The XRD results for the same samples but after three days in SBF immersion are shown in figure 34. All samples, apart from 4BHt₁, showed the appearing of a broad peak in the 2θ below 30°, which can be attributed to the appearance of amorphous calcium oxides, since the EDS results showed no traces of magnesium on the surface and the ratio Ca/P is slightly above 1.6, remaining some calcium for the formation of other compounds. Despite having shown a poor efficiency in protecting the substrate, as will be seen in the next section, 4BHt₁ displayed a high degree of crystallinity, and it does not show a disorganised band on the low 2θ region like the other samples, were, according to the RRUFF diffractograms database, is the higher intensity peak of brucite, (18.80°).

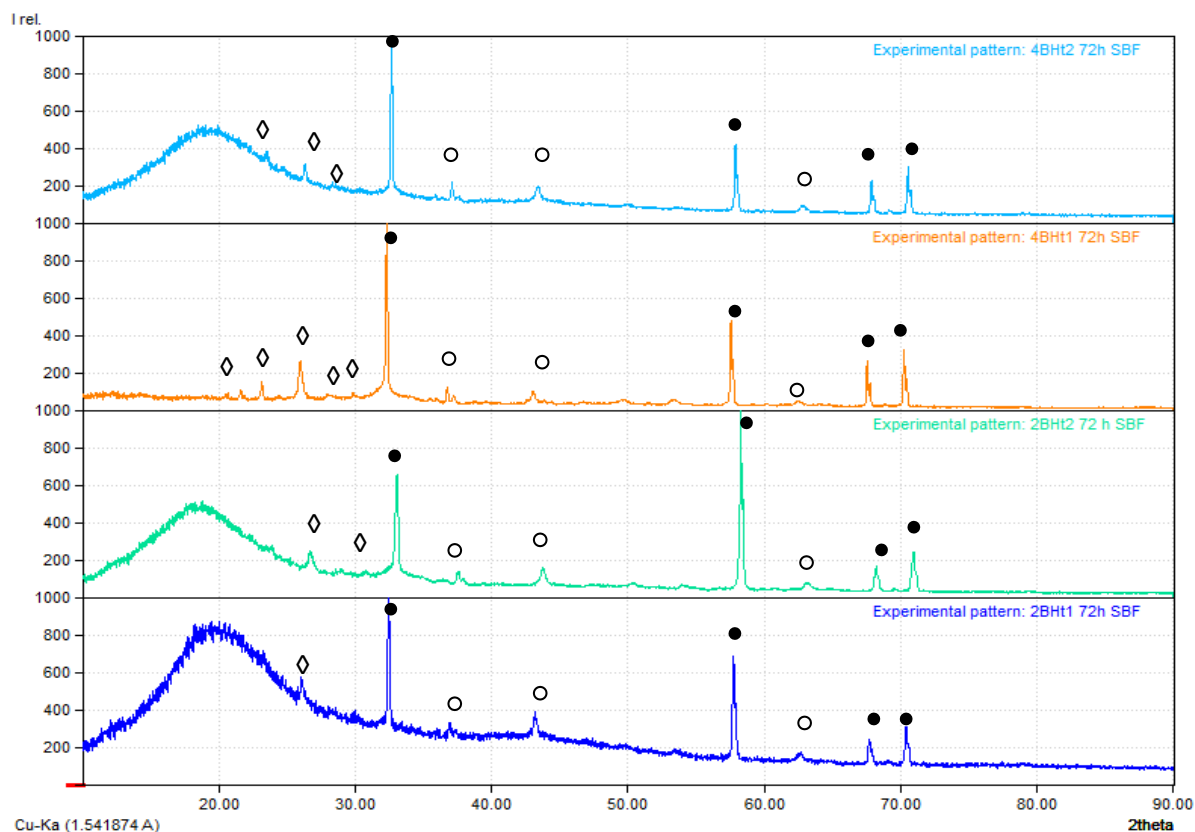


Figure 34 - XRD diffractograms of Ht samples after the immersion test; ◊ - HAp; ● - α -Mg; ○ - MgO; □ - $Mg(OH)_2$.

7.3. Electrochemical Behaviour

7.3.1. Immersion in 0.1M NaCl and EIS

The EIS characteristics of the samples coated before the Ht treatment, as well as the bare AZ31 alloy, were tested at open circuit potential after 24 hours of immersion in a 0.1M NaCl solution. Figures 35 to 50 show magnified images of all samples before and after the immersion. Evaluating those images, one can see that samples 1A, 1B, 2A, 3A, 3B and 4A show some corrosion damage after immersion, suggesting that the two most resistant samples are the 2B and 4B. which is expectable, since both were made with the concentrated electrolyte (provide a higher concentration of electrolyte species for the melted magnesium to react with and a higher conductivity, decreasing the overall voltages, augmenting the thickness and density of the barrier layer) and higher current densities that increase the overall voltages, making more magnesium to melt and be expelled through the discharge channels, increasing the coating thickness. In fact, those results suggest that an optimum value for overall voltage provides a better corrosion resistance.

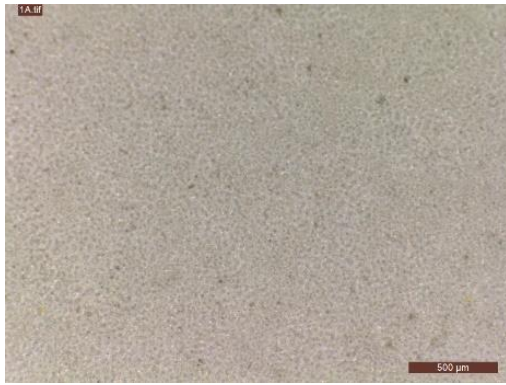


Figure 35 – Picture of sample 1A before the 24h immersion in 0.1M NaCl



Figure 36 - Picture of sample 1A after the 24h immersion in 0.1M NaCl



Figure 37 - Picture of sample 1B before the 24h immersion in 0.1M NaCl

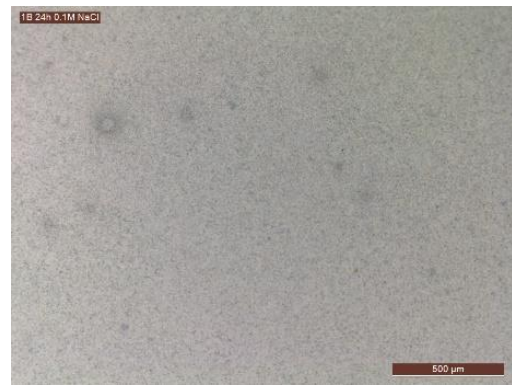


Figure 38 - Picture of sample 1B after the 24h immersion in 0.1M NaCl



Figure 39 - Picture of sample 2A before the 24h immersion in 0.1M NaCl



Figure 40 - Picture of sample 2A after the 24h immersion in 0.1M NaCl

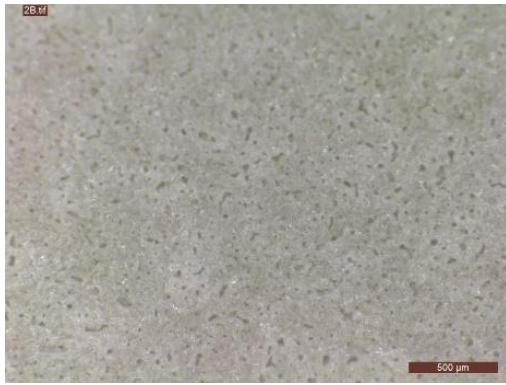


Figure 41 - Picture of sample 2B before the 24h immersion in 0.1M NaCl



Figure 42 - Picture of sample 2B after the 24h immersion in 0.1M NaCl

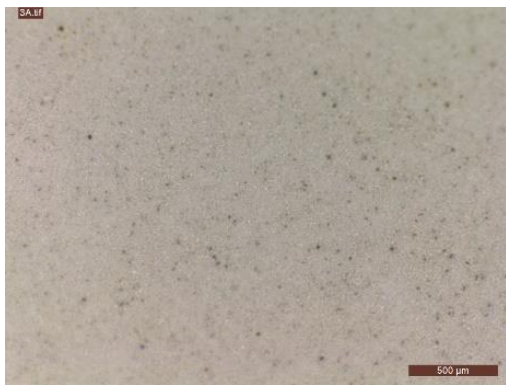


Figure 43 - Picture of sample 3A before the 24h immersion in 0.1M NaCl



Figure 44 - Picture of sample 3A after the 24h immersion in 0.1M NaCl



Figure 45 - Picture of sample 3B before the 24h immersion in 0.1M NaCl



Figure 46 - Picture of sample 3B after the 24h immersion in 0.1M NaCl

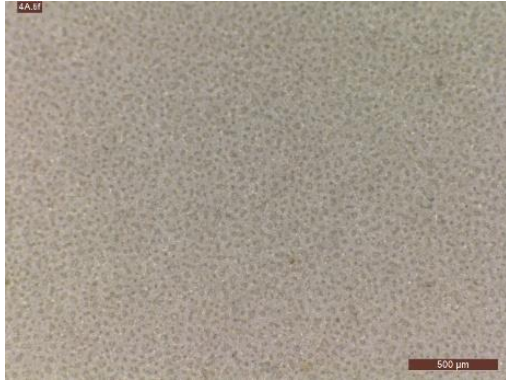


Figure 47 - Picture of sample 4A before the 24h immersion in 0.1M NaCl

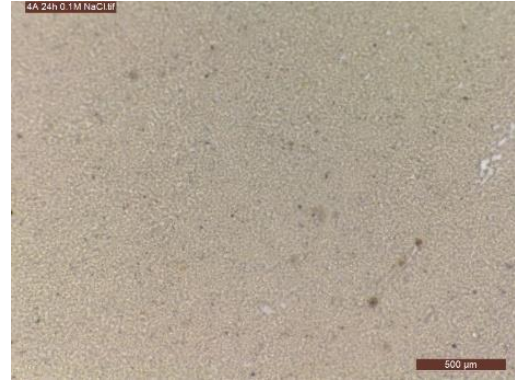


Figure 48 - Picture of sample 4A after the 24h immersion in 0.1M NaCl

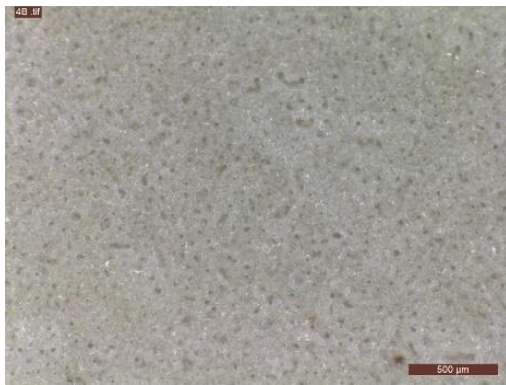


Figure 49 - Picture of sample 4B before the 24h immersion in 0.1M NaCl



Figure 50 - Picture of sample 4B after the 24h immersion in 0.1M NaCl

The Nyquist and Bode plots are shown in figures 51 and 52, respectively. The impedance response in all coated samples increases at least one order of magnitude with respect to the bare material, suggesting an accentuated increase in corrosion resistance, as expected, the samples subjected to the higher current intensity, presented a higher impedance response, as one can see from the impedance spectra below, figure 51. The fact that the coated samples did not show any inductive behaviour, typical or bare magnesium, suggests an efficient barrier effect of the coating. It is worth to note that the bare AZ31 sample has shown this inductive behaviour, seen in the insert of figure 51.

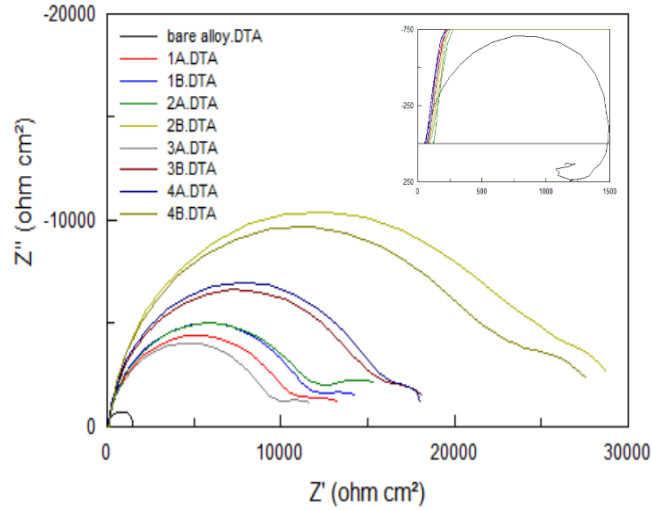


Figure 51 - Nyquist plots of bare metal and coated samples.

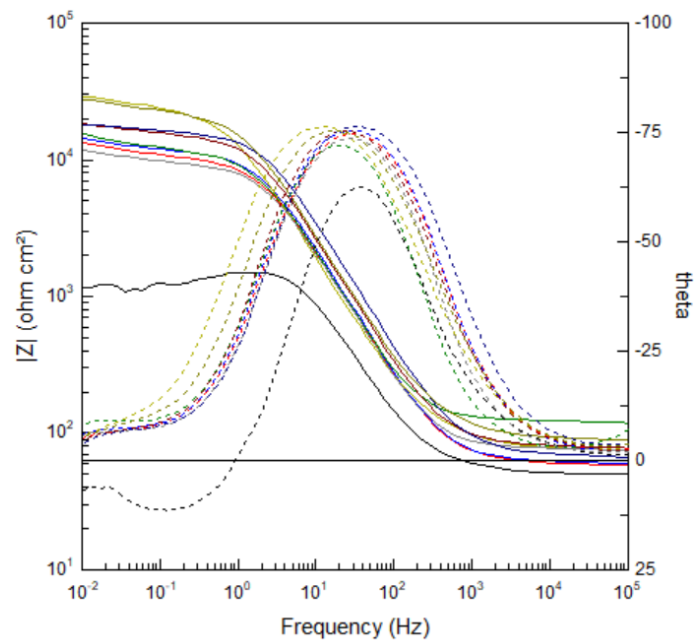


Figure 52 - Bode plots of bare metal and MAO coated samples.

Comparing samples coated in dilute electrolytes with the concentrated ones, as it was previously explained, the coating produced in the concentrated electrolytes, was denser, hence those showed a higher impedance response. The Bode plots presented in figure 52, show two different behaviours, one for the bare alloy and the other for all coated specimens.

For the bare alloy, the material is expected to corrode freely, the oxidation reaction involving adsorption of the reaction intermediates. Thus, two time constants are expected, one related to the double layer capacitance and to the charge transfer resistance, corresponding to a semicircle in the Nyquist plot, and

the other relative to the adsorption process, resulting in an inductive loop in the Nyquist plot. The equivalent circuit proposed in this case is shown in figure 53, being constituted of a CPE, accounting for the double layer capacitance, in parallel with the contribution of the faradaic processes, i.e., the charge transfer resistance, accounting for the corrosion reaction, in series with contribution of the adsorption of intermediates and respective inductive behaviour [58].

There is some controversy about the origin of the inductive behaviour present in the low frequencies region. Some authors say that it is due to the time needed for the relaxation of the adsorbed species on the substrate surface [59], whereas others propose that the inductive behaviour arises from the presence of intermediate species in the corrosion reaction of magnesium close to the substrate, meaning that before the formation of Mg^{2+} , the oxidation of Mg happens in several steps, and close to the surface, de-electronation of Mg^+ into Mg^{2+} , for example, is not taken into account by the measurement equipment, and, because the presence of intermediate species can accelerate the overall reaction, the impedance values can decrease to negative values, and since this events require time to occur, those events would only have influence in the low frequencies region [60]. Because there is no physical meaning of an inductor in an electrochemical system, in this work the inductive loop is simulated through the use of a negative resistance in parallel with a negative capacitor, the first one being explained by the decrease of charge transfer resistance on the sites close to where those intermediate species are adsorbed, and the negative capacitance created by the adsorbed species, that tend modify the double-layer properties. The values are presented in table 17.

When a pseudo-inductive behaviour is present, it should be addressed properly, as in this case the use of R_{ct} alone would lead to an underestimation of the real corrosion rate of magnesium.[60]

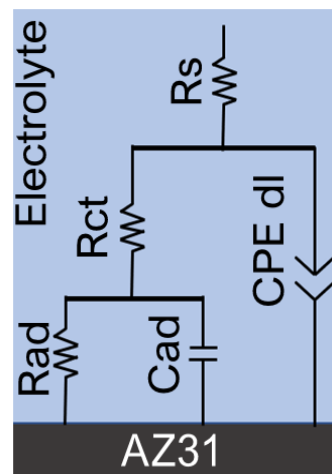


Figure 53 - Equivalent circuit proposed for the bare alloy.

For the coated materials, the Nyquist plots show two semicircles and the Bode plots also show two time constants, one, at higher frequencies, assigned to the coating properties (with a slope of approximately

-1 in the magnitude Bode plots, suggesting the behaviour of an imperfect capacitor [20, 55]) and the other, at low frequencies, linked to the corrosion processes taking place at the bottom of the coating pores. The equivalent circuit proposed to fit all the MAO coated samples is displayed in figure 54, in which, R_s represents the bulk electrolyte resistance, R_{po} is the additional ohmic resistance of the electrolyte in the MAO coating pores, R_{ct} and CPE_{dl} are, respectively, the charge transfer resistance and the double layer capacitance on the substrate/electrolyte interface in the bottom of the pores and CPE_{peo} is the constant phase element that accounts for the capacitance of the coating, taking into account the surface inhomogeneities, hence the depression on the capacitive loop in the Nyquist plots. According to this model, the coatings resistance is ignored, this happens so because its value is several orders of magnitude higher than the other resistances, so all the current measured in this experiment is mainly due to the existence of pores. And finally, figure 55 displays the fitting results of samples 2B and 4B.

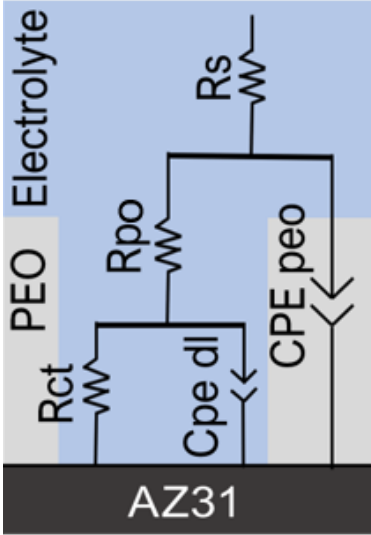


Figure 54 - Equivalent circuit proposed for all the coated samples.

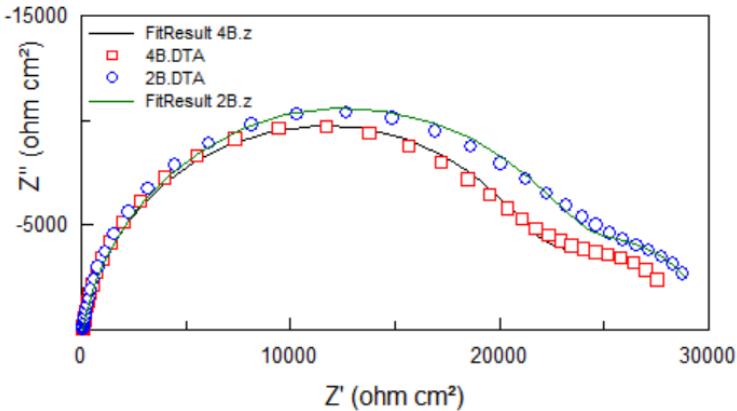


Figure 55 - Fitting results for sample 4B (red) and 2B (Blue).

The results of the fitting parameters are displayed on table 17, it is important to refer that due to the instability and reactivity of the bare alloy, EIS plots show a big amount of noise, mainly in the low frequencies region, which make it hard to find a suitable fit model for this system, hence some points in the low frequencies that clearly were the result of such noise were deleted.

The corrosion behaviour of the samples is related with their charge transfer resistance, R_{ct} [62]. All the coated samples exhibited a corrosion resistance more than one order of magnitude higher. Meaning that all the coatings were efficient in protecting the metal. All the coatings prepared with program B showed higher impedances than the coatings prepared with the program A, due to their relative thicker coatings. Comparing the two higher impedances obtained, the order was $2B > 4B$. However, because the difference between those coatings is relatively small, and as it was previously said, electrochemically, magnesium is very unstable, one cannot affirm that any of those samples had a better or worst behaviour when compared to each other.

Table 17 - Fitting results for the bare alloy and coated samples.

	Bare	1A	1B	2A	2B	3A	3B	4A	4B
R_s (Ωcm^2)	23.12	60.18	61.9	122.9	82.53	77.29	82.4	70.05	94.35
R_{po} ($\text{k}\Omega\text{cm}^2$)	-	10.17	11.23	11.13	24.95	9.03	15.09	15.71	22.89
R_{ct} ($\text{k}\Omega\text{cm}^2$)	0.73	3.84	4.51	8.08	4.74	4.18	4.26	3.91	5.44
CPE peo-T ($\mu\text{Fcm}^{-2}\text{s}^p$)	-	10.4	9.52	9.99	12.5	10.0	8.20	6.15	8.57
CPE peo-P	-	0.915	0.924	0.925	0.895	0.928	0.919	0.921	0.898
CPEdl-T ($\mu\text{Fcm}^{-2}\text{s}^p$)	53.4	962	1039	692	1300	1010	1100	1110	979
CPEdl-P	0.90	0.725	0.719	0.618	0.997	0.627	0.789	0.773	0.970
C_{ad} (mFcm^{-2})	-1.18	-	-	-	-	-	-	-	-
R_{ad} ($\text{k}\Omega\text{cm}^2$)	-0.26	-	-	-	-	-	-	-	-
χ^2 (10^{-3})	8.63	1.59	1.28	3.19	6.22	0.86	2.46	3.00	5.91
Sum of squares	0.60	0.192	0.155	0.386	0.678	0.104	0.297	0.364	0.717

7.3.2. Immersion in SBF and EIS of PEO coated samples

The two samples that showed a better corrosion resistance in the previous impedance tests, 2B and 4B, were chosen for an immersion test in SBF for 72 hours, before and after the hydrothermal treatment. Figures 57 to 65 display their macroscopic look. In all samples, macroscopically, the immersion in SBF didn't induce significant changes on the coating (macroscopically), however, in all samples except for 2BHt₁ and 4BHt₂, a localized attack occurred on their surfaces, probably inside a larger pore on the previous MAO coating, or due to the adsorption of an insolubilized particle of the PEO electrolyte on the substrate surface, keeping the PEO coating from being formed on that spot. Resulting in the samples being corroded during the hydrothermal treatment. The corrosion that happens during the treatment removed the material required for the coating support on the surface thus enlarging the hole seen on the coating. The appearance of those holes suggests a probabilistic character on the efficiency of both the plasma anodization and the following hydrothermal treatment.

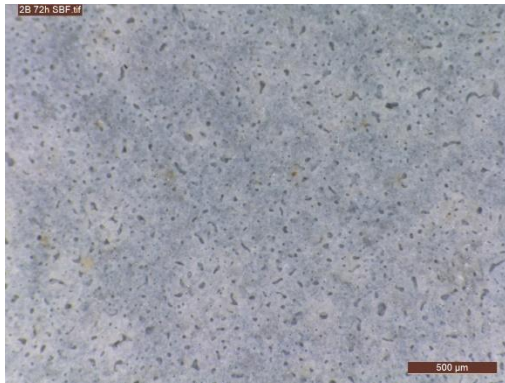


Figure 56 - 2B after the 72h immersion in SBF

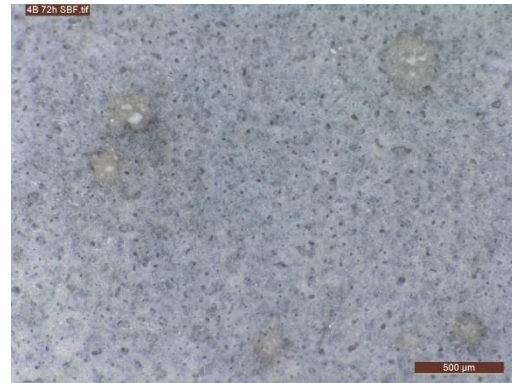


Figure 57 - 4B after the 72h immersion in SBF

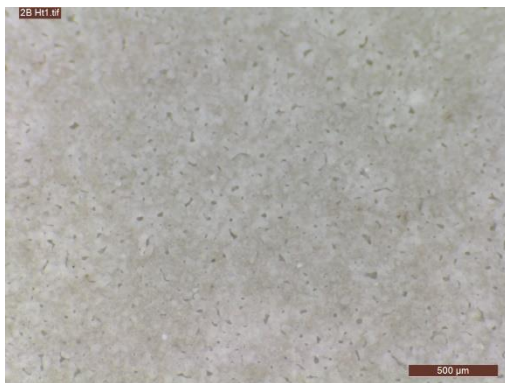


Figure 58 – 2BHt₁ before the 72h immersion in SBF



Figure 59 – 2BHt₁ after the 72h immersion in SBF

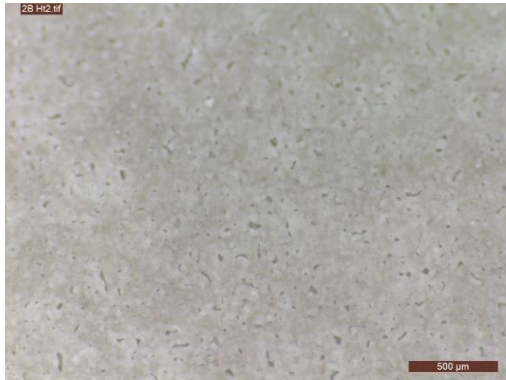


Figure 60 – 2B Ht_2 before the 72h immersion in SBF



Figure 61 – 2B Ht_2 after the 72h immersion in SBF



Figure 62 – 4B Ht_1 before the 72h immersion in SBF



Figure 63 – 4B Ht_1 after the 72h immersion in SBF

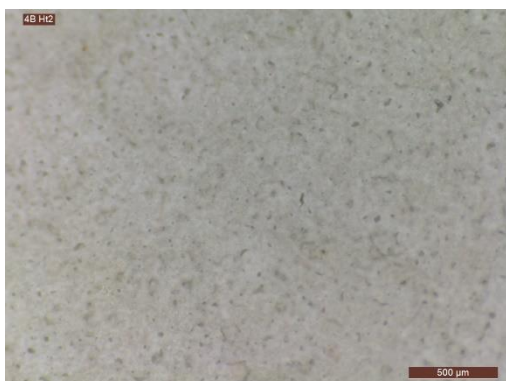


Figure 64 – 4B Ht_2 before the 72h immersion in SBF



Figure 65 – 4B Ht_2 after the 72h immersion in SBF

The open circuit potential curves of samples 2B and 4B during the first twelve hours of immersion are shown in figure 66. During the first five minutes, there is an accentuated decrease from -1.79V to -1.81V in the sample 2B potential, and from -1.78V to -1.82V in the case of 4B, associated with the penetration

of electrolyte in the coating pores. After that, the rapid shift in the noble direction implies that the electrolyte starts to interact with the denser layer of the MAO coating. After approximately one hour, both samples present a relatively stable potential, between -1.52 and -1.53V for sample 2B and -1.58 and -1.55V for sample 4B, which indicates that the electrochemical reactions occurring between the solution and the coating are happening with a slow rate, suggesting that the coating pores were partially sealed by the corrosion products, and therefore a stable and saturated state.[33]

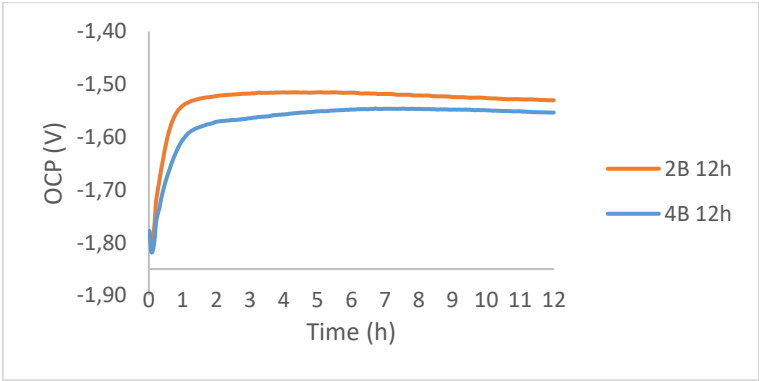


Figure 66 – 12h OCP for samples 2B and 4B immersed in SBF

Figure 67 displays the OCP curve measured for one hour before each impedance. All curves display a stable behaviour, indicating that the coatings weren't breached. Also, both samples present a small shift in potential between the first twelve hours and the end of the first day. By the end of the second day, both samples had a small decrease in potential, and at the end of the 72 hours, both potentials had a substantial shift towards the noble direction, indicating the deposition of electrolyte species inside coating pores, decreasing their size.

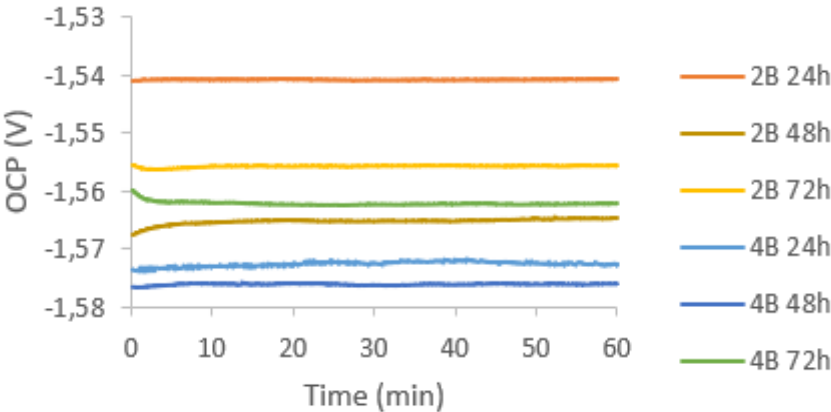


Figure 67 – OCP curve one hour before each EIS in sample 2B and 4B

The Nyquist and Bode plots of the MAO samples immersed in SBF solution for three days is shown in figures 68 to 71. In both samples is observed an accentuated decrease in impedance between the first 12h and the end of the first day, after that the decrease is less accentuated, and in the case of sample

4B there is an increase in the last 24 hours, suggesting the appearance of a protective film, or the formation of a stable MgO phase on the pores bottom.

All the Nyquist plots show two capacitive loops in the high and medium frequencies, one in the low and an inductive one also in the low frequencies region. The capacitive loops are the result the capacitance of the MAO coating, and the substrate double layer capacitance. In both samples, the 72h impedance spectra and phase angle plot suggest the appearance of a fourth time constant in the high frequencies region, result of a competition between the dissolution and formation of compounds on the coatings surface, which is more accentuated on sample 2B than sample 4B. However, the introduction of another CPE on the equivalent circuit would give rise to a very large fitting error, resulting in very large errors in the fitting parameters.

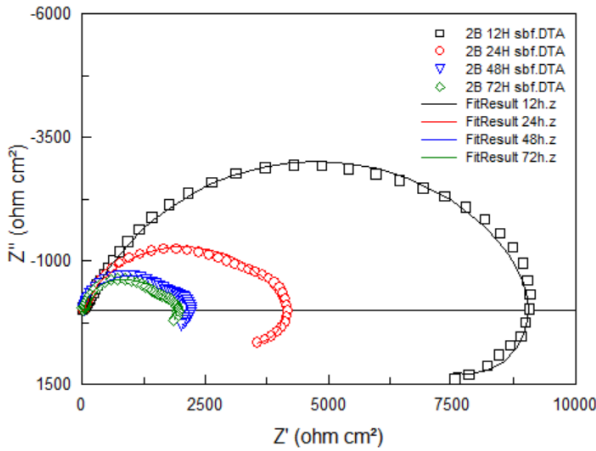


Figure 68 - 2B Nyquist plots for impedance in SBF

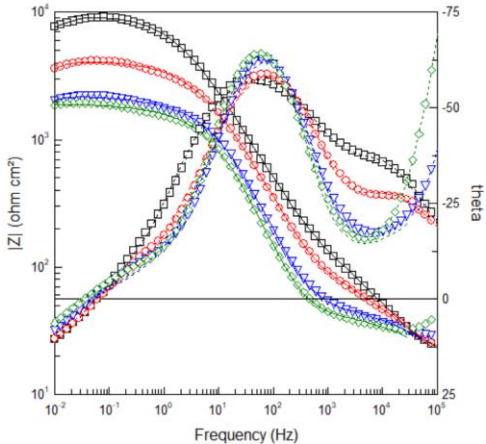


Figure 69 - 2B Bode plots for impedance in SBF

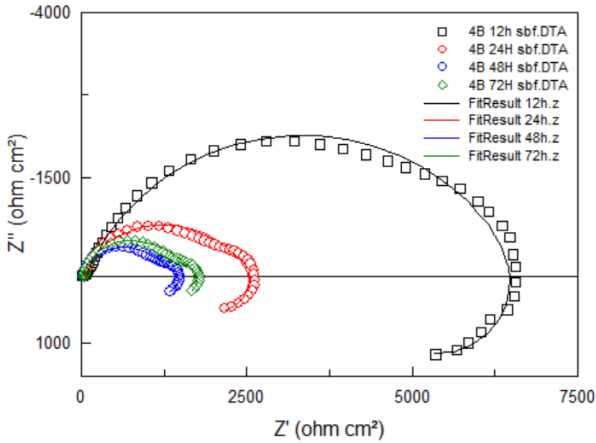


Figure 70 - 4B Nyquist plots for impedance in SBF

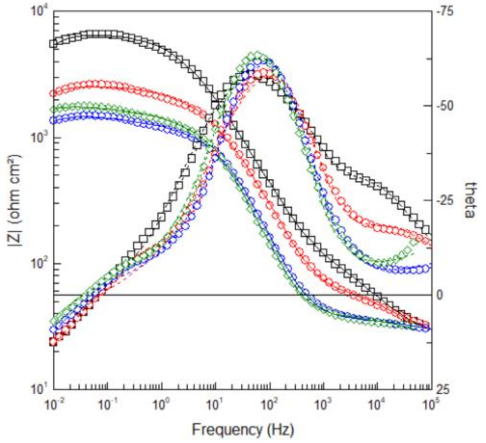


Figure 71 - 4B Bode plots for impedance in SBF

The electrical equivalent circuit proposed to fit the data of this two samples is shown in figure 72. This circuit is similar to the one proposed for the PEO coated samples in figure 54, however, SBF is a much more aggressive solution than a 0.1M NaCl, hence the barrier layer of the protective coatings does not provide a protection as effective as before, and an inductive behaviour is seen in the low frequencies

region, implying the existence on another time constant. In this circuit the negative resistance and capacitor, used to describe the contribution of adsorbed or intermediate species on the metals surface on the bare alloy equivalent circuit is added in parallel to the charge transfer resistance of the circuit proposed for the PEO coated samples in the NaCl solution.

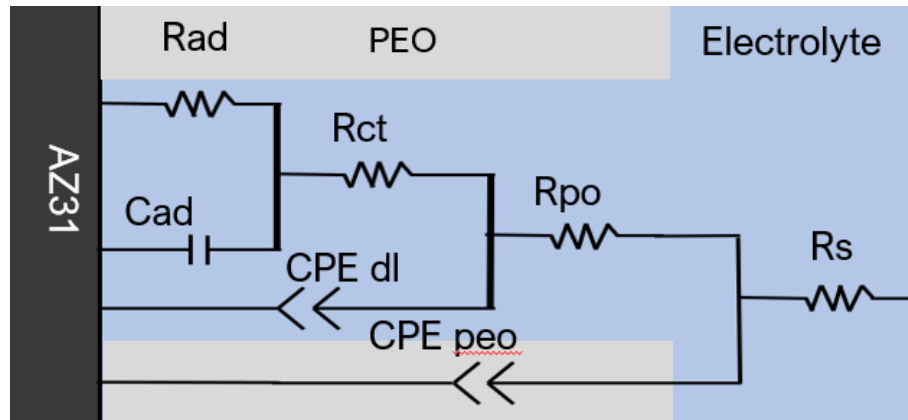


Figure 72 - Equivalent circuit proposed to fit the data of samples 2B and 4B immersed in SBF

Table 18 - Equivalent circuit fitting results

	2B 12h	2B 24h	2B 48h	2B 72h	4B 12h	4B 24h	4B 48h	4B 72h
Rpo (Ωcm^2)	156.8	100.2	55.21	48.19	140.50	59.19	40.09	42.16
Rct ($\text{k}\Omega\text{cm}^2$)	9.32	4.12	2.20	1.92	6.57	2.53	1.58	1.84
Rad ($\text{k}\Omega\text{cm}^2$)	-3.00	-1.48	-0.83	-1.18	-2.52	-1.10	-0.60	-0.69
CPE peo-T ($\mu\text{Fcm}^{-2}\text{s}^p$)	10.81	26.18	47.32	59.03	16.04	35.10	111.27	88.13
CPE peo-P	0.69	0.61	0.48	0.57	0.66	0.59	0.33	0.38
CPEdl-T ($\mu\text{Fcm}^{-2}\text{s}^p$)	8.44	4.19	9.56	11.42	5.77	3.99	12.53	13.79
CPEdl-P	0.76	0.92	0.95	0.969	0.84	0.96	0.94	0.95
Cad (mFcm^{-2})	-0.38	-11.50	-32.54	-55.33	-5.520	-17.46	-30.95	-41.37
$\chi^2 (10^{-3})$	0.39	1.35	4.11	6.88	1.05	3.11	2.73	2.73
Sum of squares	0.05	0.16	0.48	0.75	0.13	0.37	0.32	0.31

7.3.3. Immersion in SBF and SBF of Hydrothermally treated samples

The OCP curves of the first twelve hours of immersion in SBF of samples 2BHt₁ and 4BHt₂ are displayed on Figure 73. During the first seven hours, sample 2BHt₁ showed a relatively instable behaviour, this may be due to the porous and inhomogeneous nature of the coating, and a competition between the dissolution and formation of new protective layers such as hydroxyapatites. After seven hours, the OCP becomes stable, with a small slope towards the noble direction, indicating the existence on a steady state between the electrolyte and the coating. Sample 4BHt₂, on the other hand, started with a potential drop, during the first hour, probably due to the dissolution and rearrangement of protective layers, but after the first hour, the potential starts being shifted towards less negative values, indicating also, the growing or thickening of the present coating and the reaching of a steady state.

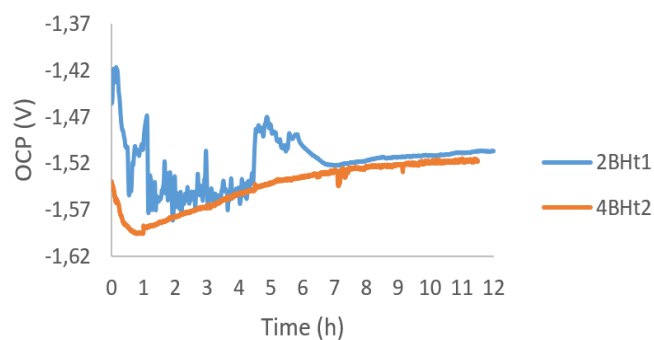


Figure 73 - 12h OCP for samples 2bh_{t1} 4bh_{t2} immersed in SBF

The OCP measured at the last hour of the first, second and third day, of sample 2BHt₁ reveal a stable behaviour, indicating that dissolution and formation of protective layers in the steady state, and it has approximately the same value of around -1.5V during the first 48th hours. By the end of the third day the OCP increased, reaching the -1,46V, indicating that the coating is improving its protection over time. In the case of sample 4BHt₂, however, the first day, the OCP remains around -1.53V, and in the last two days, the potential had a small decrease of about 0.1V, and remained almost unchanged for the last 24 hours, indicating also the existence of an equilibrium between the electrolyte and the coating.

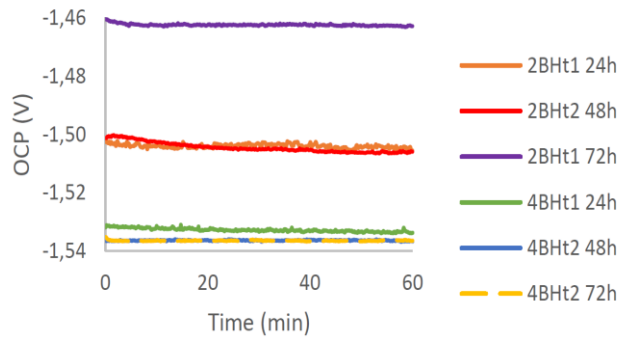


Figure 74 - OCP curve one hour before each EIS in sample 2Bht₁ and 4Bht₁

Since the hydrothermal treatment performed on samples 2B and 4B adds another layer on the protective coatings, the EIS results also display one more time constant, as in figures 75 and 77, the Nyquist plots display three capacitive loops and one inductive. The first capacitive loop appears in the high frequencies region, probably due to the first layer of the coating, between the porous MAO and the electrolyte, the second capacitive loop appears also in the high frequencies region, and it is related with the MAO coating, beneath the hydroxyapatite layer. The third one results from the inner denser layer typical from anodization treatments, and the inductive loop, as explained before, results from the adsorption of intermediate species in the corrosion reactions. Sample 2Bht₁ displays a larger capacitance and resistance, as expected since in the OCP curves above it exhibits a more noble behaviour. Despite of the suggestion of interaction between the substrate and the electrolyte given by the inductive loop, the impedance behaviour does not change shape in the three days of immersion. Meaning that the coating is relatively resistant in a physiological environment. Sample 4Bht₂ also presents the same behaviour that sample 2Bht₁, however, the Nyquist spectra of figure 77 show a bit higher impedance at 72 hours than at 48, implying that in this environment, the coatings pores are being sealed through the growing of a new layer of calcium phosphates.

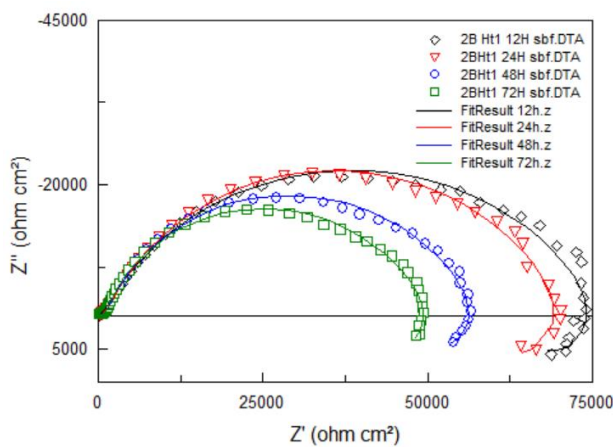


Figure 75 - 2Bht₁ Nyquist plots for impedance in SBF

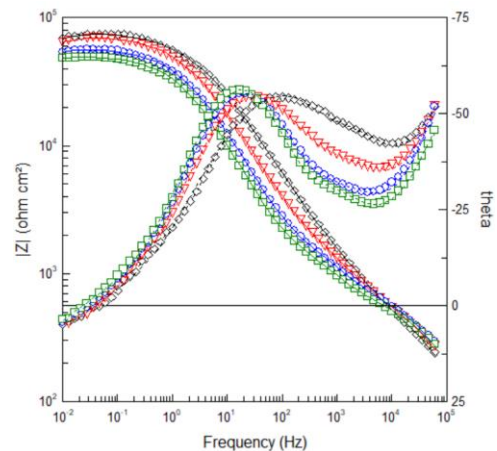


Figure 76 - 2Bht₁ Bode plots for impedance in SBF

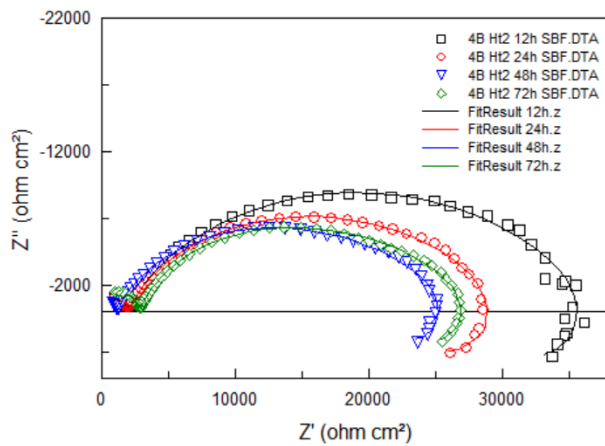


Figure 77 - 4BHt₂ Nyquist plots for impedance in SBF

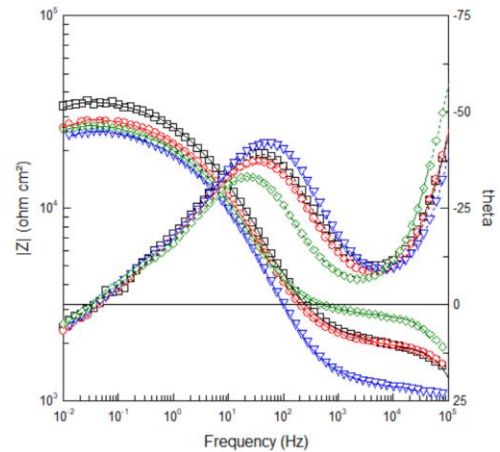


Figure 78 - 4BHt₂ Bode plots for impedance in SBF

The phase angle plots in figures 76 and 78 present a similar behaviour in both samples. The phase angle diagrams present four time constants, two in the high frequencies region, one in the middle and one in the low. The Bode plots in figures 76 and 78, however, display a slightly different response, in sample 2BHt₁, the impedance modulus increases in a faster rate since the higher frequency point, and the 4BHt₂ presents a plateau between the 10⁵ and 10³ Hz, meaning that in the first case the substrate is protected from the electrolyte, and the coatings capacitance dominates the overall impedance values. In the case of sample 4BHt₂, the plateau in the high frequencies region suggests the existence of a larger contribution of electrolyte and charge transfer resistances, meaning a less efficient protection.[46] On the other hand, the impedance measured at 72 hours of immersion on sample 4BHt₂ displays an evolution towards a behaviour similar to sample 2BHt₁. Meaning that despite of being less efficient in protection of the alloy, 4BHt₂ coating exhibits a faster rate in growing a protection layer.

The equivalent circuit proposed to fit the impedance results is shown in figure 79, and the fitting results are shown in table 19. In this circuit, CPEHAp represents the coating's top layer, created by the hydrothermal treatment. The RHAp represents the pores in this layer. The rest of the circuit is similar to the one proposed for the PEO coatings fitting in SBF.

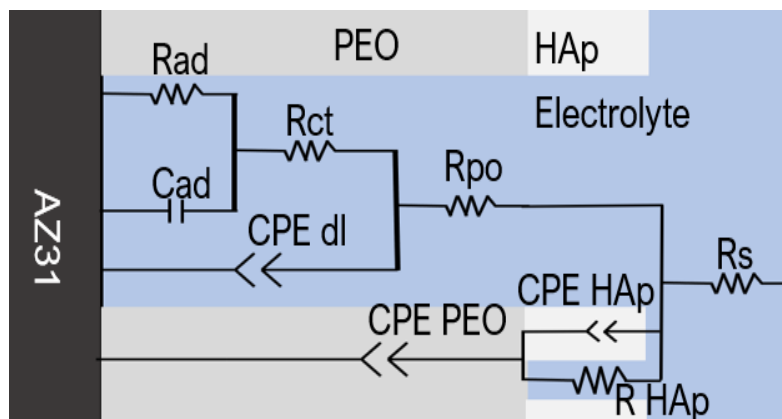


Figure 79 - Equivalent circuit proposed for fitting impedance data of samples 2BHt₁ and 4BHt₂.

Both samples presented a charge transfer resistance one order of magnitude higher than the MAO coated samples, implying that the protection provided by the hydrothermal treatment was effective in decreasing the porosity in all samples, thus reducing the area exposed to the electrolyte, which substantially decreased the corrosion rate.

Table 19 - Fitting results for samples 2BHt₁ and 4BHt₂

	2BHt ₁ 12h	2BHt ₁ 24h	2BHt ₁ 48h	2BHt ₁ 72h	4BHt ₂ 12h	4BHt ₂ 24h	4BHt ₂ 48h	4BHt ₂ 72h
RpHAp (Ωcm²)	206.40	318.50	427.50	493.5	2440	3526	3498	5853
Rpo (Ωcm²)	10161	3899	2756	2741	6367	3791	1577	4733
Rct (kΩcm²)	67.70	68.47	56.06	48.56	31.80	27.56	26.61	24.72
Rad (kΩcm²)	-14.21	-14.53	-11.59	-11.74	-8.86	-8.09	-6.84	-6.64
CPEHAp-T (Fcm⁻²s^p)(10⁻⁸)	5.64	6.69	6.32	14.88	0.11	0.11	0.17	0.11
CPEHAp-P	0.91	0.88	0.87	0.79	0.99	0.99	1.00	1.00
CPE peo-T (μFcm⁻²s^p)	2.11	2.15	2.80	3.47	5.46	6.23	7.86	7.46
CPE peo-P	0.64	0.64	0.63	0.64	0.55	0.51	0.43	0.47
CPEdl-T (Fcm⁻²s^p)(10⁻⁸)	7.63	64.36	108.13	113.92	28.33	83.90	785.56	126.43
CPEdl-P	0.94	0.84	0.86	0.90	0.93	0.83	0.80	0.84
Cad (mFcm⁻²)	-0.83	-1.05	-1.62	-2.44	-1.77	-1.57	-1.61	-2.17
X² (10⁻³)	0.65	0.64	0.73	0.34	0.88	0.19	0.11	0.24
Sum of squares	0.07	0.07	0.08	0.04	0.10	0.02	0.01	0.03

8. Conclusions and future work

Materials used nowadays for bone implant applications present several hazardous effects in the human body, like the stress shielding effect and the release of toxic substances into the body, typical of metals, or the high degradation rate and the low Young modulus of polymers, or the brittleness and low toughness of ceramics.

All those disadvantages present a challenge in finding an efficient material resistant enough to withstand all the bone implants challenges and biodegradable at a controllable rate.

Magnesium potential as a biomaterial for implants is well known for some time now, however its high corrosion rate keeps it from being used.

In this work, several chemical compositions of PEO coatings and two for hydrothermal treatments on top of those were proposed to coat AZ31 alloy aiming to improve its performance as a biomaterial. Those were tested in terms of morphology and biological performance. The thickness, morphology, and phase distribution by were tested by an Eddy current thickness gauge, SEM coupled with EDS analysis and XRD, respectively. The corrosion performance was tested by EIS both in 0.1M NaCl aqueous solution and SBF, and OCP measurements in SBF.

The results of the present work related with the PEO coatings are summarized here:

- Plasma electrolytic anodization produces a thick porous coating composed of oxides/hydroxides on the sample surface, and the thickness and porosity of such coating increases with the increase of both solution concentration and current intensity.
- EIS in 0.1 NaCl solution revealed that thicker coatings with denser barrier layers increase the alloy corrosion resistance for, at least, one order of magnitude by substantially diminishing the exposed area.
- The effectiveness of the PEO coatings protection was also confirmed by the absence of inductive behaviour in the NaCl solution EIS.
- Immersion in SBF decreases, slightly, the pores diameter by deposition of electrolyte species.
- OCP measurements in SBF revealed, at first, the deposition and formation of a protective film, and after, an equilibrium between dissolution and formation of such films. Resulting in an increasing corrosion resistance with time due to the slight decrease in the pores diameter.
- EIS in SBF showed an extra time constant in the low frequencies region, due to the aggressivity of the chlorides concentration in the solution and confirmed the OCP results that the samples corrosion resistance increases with time.
- PEO sample made with KOH (2B) showed a higher corrosion resistance in all impedances, however, the sample made with $\text{Ca}(\text{OH})_2$ (4B) displayed a higher increase in corrosion resistance.
- SBF immersion decreased the thickness of sample 2B and increased the thickness of sample 4B, suggesting that in spite of being more protective, sample 2B has showed an inferior apatite forming ability.

- The efficiency of this coating is highly dependent of hydrodynamic conditions.

The results related with the hydrothermal treatment made on top of the selected PEO coated samples is listed below:

- The hydrothermal treatment after on top of the PEO coating slightly increases the thickness and decreases the pore diameter and density on the coating through the precipitation and nucleation of needle-like hydroxyapatite structures on the PEO surface.
- OCP measurement reveals a competition between dissolution and formation of a protective film, that after, it reaches an equilibrium.
- EIS revealed another time constant belonging to the hydroxyapatite layer on top of the PEO one, confirming the existence of a new protective layer.
- SBF immersion decreases the crystallinity degree of the coating, making it more similar to actual bone.
- EIS evolution with time suggests that in spite of being more corrosion resistant, sample 2BHT₁ as well as sample 2B, showed a smaller apatite forming ability.

Related with this work, an evaluation of the corrosion behaviour by another method, like potentiodynamic polarization, or hydrogen evolution is vital so the mass loss per time could be obtained, further research in cell attachment, osteoconductive and immersion in SBF for longer periods is needed.

The substantial improves of AZ31 alloy corrosion resistance, in physiological conditions, with out the use of any toxic element besides the aluminium present in the alloy proofs that the production of biodegradable bone implants is not far from reality.

Improvements to the results obtained here would be a coating produced in an electrolyte with substances more soluble, to decrease the hydrodynamic conditions influence on the overall results, an alloy with out any toxic substances, like Mg-Ca.

9. References

- [1] D. G. Poitout, *Biomechanics and Biomaterials in Orthopedics*. 2004.
- [2] F. Haddad and a Cohen, *Joint Replacement*, no. July. 2009.
- [3] Z. Sheikh, S. Najeeb, Z. Khurshid, V. Verma, H. Rashid, and M. Glogauer, "Biodegradable materials for bone repair and tissue engineering applications," *Materials (Basel)*, vol. 8, no. 9, pp. 5744–5794, 2015.
- [4] E. García-Gareta, M. J. Coathup, and G. W. Blunn, "Osteoinduction of bone grafting materials for bone repair and regeneration," *Bone*, vol. 81, pp. 112–121, 2015.
- [5] M. Saini, "Implant biomaterials: A comprehensive review," *World J. Clin. Cases*, vol. 3, no. 1, p. 52, 2015.
- [6] F. Witte, "Reprint of: The history of biodegradable magnesium implants: A review," *Acta Biomater.*, vol. 23, no. 5, pp. S28–S40, 2015.
- [7] D. Zhao, F. Witte, F. Lu, J. Wang, J. Li, and L. Qin, "Current status on clinical applications of magnesium-based orthopaedic implants: A review from clinical translational perspective," *Biomaterials*, vol. 112, pp. 287–302, 2017.
- [8] S. Agarwal, J. Curtin, B. Duffy, and S. Jaiswal, "Biodegradable magnesium alloys for orthopaedic applications: A review on corrosion, biocompatibility and surface modifications," *Mater. Sci. Eng. C*, vol. 68, pp. 948–963, 2016.
- [9] M. G. G. K. Meenashisundaram, T. S. N. S. Narayanan, I.-S. Park, and M.-H. Lee, *Insight into Designing Biocompatible Magnesium Alloys and Composites: Processing, Mechanical and Corrosion Characteristics*, vol. 44, no. 8. 2014.
- [10] G. Eddy, J. Poinern, S. Brundavanam, and D. Fawcett, "Biomedical Magnesium Alloys: A Review of Material Properties, Surface Modifications and Potential as a Biodegradable Orthopaedic Implant," *Am. J. Biomed. Eng.*, vol. 2, no. 6, pp. 218–240, 2012.
- [11] G. Song, "Control of biodegradation of biocompatible magnesium alloys," *Corros. Sci.*, vol. 49, no. 4, pp. 1696–1701, 2007.
- [12] A. Popoola, O. Olorunniwo, and O. Ige, "Corrosion Resistance Through the Application of Anti-Corrosion Coatings," in *Developments in Corrosion Protection*, 2014.
- [13] P. R. Roberge and R. Pierre, *Handbook of Corrosion Engineering Library of Congress Cataloging-in-Publication Data*. 1999.
- [14] R. Winston Revie and H. H. Uhlig, *Corrosion and Corrosion Control: An introduction to corrosion science and engineering*, vol. 7. 2008.
- [15] P. A. Schweitzer, *Fundamentals of Corrosion-Mechanisms, Causes, and Preventative Methods*, vol. 53, no. 9. 2013.
- [16] P. Marcus, *Corrosion Mechanisms in Theory and Practice edited by*. 2002.
- [17] G.-L. Song, *Corrosion prevention of magnesium alloys*, no. 1. 2014.
- [18] R. Baboian, S. W. D. Jr., H. P. Hack, E. L. Hibner, and J. R. Scully, "Corrosion Tests and Standards: Application and Interpretation--Second Edition." pp. 1–886, 2009.
- [19] J. B. Bushman, "Calculation of Corrosion Rate from Corrosion Current (Faraday ' s Law) by,"

Corrosion, pp. 7–10, 2002.

- [20] R. G. Kelly, J. R. Scully, D. W. Shoesmith, and R. G. Buchheit, *Electrochemical Techniques in Corrosion Science and Engineering*, vol. 18. 2003.
- [21] W. J. Lorenz and F. Mansfeld, "Determination of corrosion rates by electrochemical DC and AC methods," *Corros. Sci.*, vol. 21, no. 9–10, pp. 647–672, 1981.
- [22] G.-L. Song, *Corrosion of Magnesium Alloys*. 2011.
- [23] M. Esmaily *et al.*, "Fundamentals and advances in magnesium alloy corrosion," *Prog. Mater. Sci.*, vol. 89, no. May, pp. 92–193, 2017.
- [24] A. Zomorodian, M. P. Garcia, T. Moura E Silva, J. C. S. Fernandes, M. H. Fernandes, and M. F. Montemor, "Corrosion resistance of a composite polymeric coating applied on biodegradable AZ31 magnesium alloy," *Acta Biomater.*, vol. 9, no. 10, pp. 8660–8670, 2013.
- [25] A. Zomorodian, C. Santos, M. J. Carnezim, T. M. E. Silva, J. C. S. Fernandes, and M. F. Montemor, "'In-vitro' corrosion behaviour of the magnesium alloy with Al and Zn (AZ31) protected with a biodegradable polycaprolactone coating loaded with hydroxyapatite and cephalixin," *Electrochim. Acta*, vol. 179, pp. 431–440, 2015.
- [26] H. Hornberger, S. Virtanen, and A. R. Boccaccini, "Biomedical coatings on magnesium alloys - A review," *Acta Biomater.*, vol. 8, no. 7, pp. 2442–2455, 2012.
- [27] C. Blawert, W. Dietzel, E. Ghali, and G. Song, "Anodizing treatments for magnesium alloys and their effect on corrosion resistance in various environments," *Adv. Eng. Mater.*, vol. 8, no. 6, pp. 511–533, 2006.
- [28] F. C. Walsh *et al.*, "Plasma electrolytic oxidation (PEO) for production of anodised coatings on lightweight metal (Al, Mg, Ti) alloys," *Trans. Inst. Met. Finish.*, vol. 87, no. 3, pp. 122–135, 2009.
- [29] J. a Curran, "Plasma electrolytic oxidation for surface protection of aluminium, magnesium and titanium alloys," *Trans. IMF*, vol. 89, no. 6, pp. 295–297, 2011.
- [30] H. Duan, C. Yan, and F. Wang, "Growth process of plasma electrolytic oxidation films formed on magnesium alloy AZ91D in silicate solution," *Electrochim. Acta*, vol. 52, no. 15, pp. 5002–5009, 2007.
- [31] L. Zhang, J. Zhang, C. fu Chen, and Y. Gu, "Advances in microarc oxidation coated AZ31 Mg alloys for biomedical applications," *Corros. Sci.*, vol. 91, pp. 7–28, 2015.
- [32] H. F. Guo, M. Z. An, H. B. Huo, S. Xu, and L. J. Wu, "Microstructure characteristic of ceramic coatings fabricated on magnesium alloys by micro-arc oxidation in alkaline silicate solutions," *Appl. Surf. Sci.*, vol. 252, no. 22, pp. 7911–7916, 2006.
- [33] H. Duan, K. Du, C. Yan, and F. Wang, "Electrochemical corrosion behavior of composite coatings of sealed MAO film on magnesium alloy AZ91D," *Electrochim. Acta*, vol. 51, no. 14, pp. 2898–2908, 2006.
- [34] Q. You, H. Yu, H. Wang, Y. Pan, and C. Chen, "Effect of current density on the microstructure and corrosion resistance of microarc oxidized ZK60 magnesium alloy," *Biointerphases*, vol. 9, no. 3, p. 31009, 2014.
- [35] Y. M. Wang, D. C. Jia, L. X. Guo, T. Q. Lei, and B. L. Jiang, "Effect of discharge pulsating on microarc oxidation coatings formed on Ti6Al4V alloy," *Mater. Chem. Phys.*, vol. 90, no. 1, pp. 128–133, 2005.

- [36] C. Huan *et al.*, "Effect of the Pulse Duty Cycle on Characteristics of Plasma Electrolytic Oxidation Coatings Formed on AZ31 Magnesium Alloy," *Chinese Phys. Lett.*, vol. 26, no. 9, p. 096802, 2009.
- [37] T. S. N. Sankara Narayanan, I. S. Park, and M. H. Lee, "Strategies to improve the corrosion resistance of microarc oxidation (MAO) coated magnesium alloys for degradable implants: Prospects and challenges," *Prog. Mater. Sci.*, vol. 60, no. 1, pp. 1–71, 2014.
- [38] R. O. Hussein, D. O. Northwood, and X. Nie, "The influence of pulse timing and current mode on the microstructure and corrosion behaviour of a plasma electrolytic oxidation (PEO) coated AM60B magnesium alloy," *J. Alloys Compd.*, vol. 541, pp. 41–48, 2012.
- [39] R. F. Zhang, G. Y. Xiong, and C. Y. Hu, "Comparison of coating properties obtained by MAO on magnesium alloys in silicate and phytic acid electrolytes," *Curr. Appl. Phys.*, vol. 10, no. 1, pp. 255–259, 2010.
- [40] H. Luo, Q. Cai, B. Wei, B. Yu, J. He, and D. Li, "Study on the microstructure and corrosion resistance of ZrO₂-containing ceramic coatings formed on magnesium alloy by plasma electrolytic oxidation," vol. 474, pp. 551–556, 2009.
- [41] R. F. Zhang, S. F. Zhang, and S. W. Duo, "Influence of phytic acid concentration on coating properties obtained by MAO treatment on magnesium alloys," *Appl. Surf. Sci.*, vol. 255, no. 18, pp. 7893–7897, 2009.
- [42] H. F. Guo and M. Z. An, "Growth of ceramic coatings on AZ91D magnesium alloys by micro-arc oxidation in aluminate-fluoride solutions and evaluation of corrosion resistance," *Appl. Surf. Sci.*, vol. 246, no. 1–3, pp. 229–238, 2005.
- [43] S. V. Dorozhkin, "Calcium orthophosphate deposits: Preparation, properties and biomedical applications," *Mater. Sci. Eng. C*, vol. 55, pp. 272–326, 2015.
- [44] S. Hiromoto and M. Tomozawa, "Corrosion Behavior of Magnesium with Hydroxyapatite Coatings Formed by Hydrothermal Treatment," *Mater. Trans.*, vol. 51, no. 11, pp. 2080–2087, 2010.
- [45] M. Tomozawa and S. Hiromoto, "Growth mechanism of hydroxyapatite-coatings formed on pure magnesium and corrosion behavior of the coated magnesium," *Appl. Surf. Sci.*, vol. 257, no. 19, pp. 8253–8257, 2011.
- [46] M. E. Orazem and B. Tribollet, *Electrochemical Impedance Spectroscopy*, vol. 48, 2008.
- [47] B. Chang and S. Park, "Electrochemical Impedance Spectroscopy," *Annu. Rev. Anal. Chem.*, vol. 3, no. 1, pp. 207–229, 2010.
- [48] E. Barsoukov and J. R. Macdonald, *Impedance Spectroscopy*. 2005.
- [49] Gamry, "Physical Electrochemistry & Equivalent Circuit Elements," *Gamry Instruments*, vol. 2, pp. 1–13, 2017.
- [50] L. Reimer, *Scanning Electron Microscopy, Physics of Image Formation and Microanalysis*, Second. .
- [51] J. I. Goldstein, D. E. Newbury, J. R. Michael, N. W. M. Ritchie, J. H. J. Scott, and D. C. Joy, *Microscopy and X-Ray Microanalysis*. 2018.
- [52] Y. Leng, "Materials Characterization," 2008.
- [53] J. Epp, *X-Ray Diffraction (XRD) Techniques for Materials Characterization*. Elsevier Ltd, 2016.

- [54] E. Aghion and G. Golub, *Production technologies of magnesium*. 2006.
- [55] T. Kokubo and H. Takadama, "How useful is SBF in predicting in vivo bone bioactivity?," *Biomaterials*, vol. 27, no. 15, pp. 2907–2915, 2006.
- [56] R. Cheng, F. Pan, S. Jiang, C. Li, B. Jiang, and X. Jiang, "Effect of Sr addition on the grain refinement of AZ31 magnesium alloys," *Prog. Nat. Sci. Mater. Int.*, vol. 23, no. 1, pp. 7–12, 2013.
- [57] P. Tian, X. Liu, and C. Ding, "In vitro degradation behavior and cytocompatibility of biodegradable AZ31 alloy with PEO/HT composite coating," *Colloids Surfaces B Biointerfaces*, vol. 128, pp. 44–54, 2015.
- [58] I. B. Singh, M. Singh, and S. Das, "A comparative corrosion behavior of Mg, AZ31 and AZ91 alloys in 3.5% NaCl solution," *J. Magnes. Alloy.*, vol. 3, no. 2, pp. 142–148, 2015.
- [59] G. Baril, G. Galicia, C. Deslouis, N. Pébère, B. Tribollet, and V. Vivier, "An Impedance Investigation of the Mechanism of Pure Magnesium Corrosion in Sodium Sulfate Solutions," *J. Electrochem. Soc.*, vol. 154, no. 2, p. C108, 2007.
- [60] L. G. Bland, A. D. King, N. Birbilis, and J. R. Scully, "Assessing the corrosion of commercially pure magnesium and commercial AZ31B by electrochemical impedance, mass-loss, hydrogen collection, and inductively coupled plasma optical emission spectrometry solution analysis," *Corrosion*, vol. 71, no. 2, pp. 128–145, 2015.
- [61] D. Liu, Y. Li, Y. Zhou, and Y. Ding, "The Preparation, Characterization and Formation Mechanism of a Calcium Phosphate Conversion Coating on Magnesium Alloy AZ91D," *Materials (Basel)*, vol. 11, no. 6, p. 908, 2018.
- [62] M. Curioni, F. Scenini, T. Monetta, and F. Bellucci, "Correlation between electrochemical impedance measurements and corrosion rate of magnesium investigated by real-time hydrogen measurement and optical imaging," *Electrochim. Acta*, vol. 166, pp. 372–384, 2015.

